On velocity profiles, stresses and Bagnold scaling of sheared granular system in zero gravity

Oleh Baran* and Lou Kondic
Department of Mathematical Sciences and Center for Applied Mathematics and Statistics,
New Jersey Institute of Technology, Newark, NJ 07102, USA
(Dated: August 1, 2004)

We report the results of three-dimensional molecular dynamics simulations of sheared granular system in a Couette geometry.[1] The simulations use realistic boundary conditions that may be expected in physical experiments. For a range of boundary properties we report velocity and density profiles, as well as forces on the boundaries. In particular, we find that the results for the velocity profiles throughout the shearing cell depend strongly on the interaction of the system particles with the physical boundaries. Even frictional boundaries can allow for significant slippage of the particles, therefore, reducing the shear in the system. Next, we present shear rate dependence of stress, including mean force and force fluctuations, both for controlled volume, and for controlled stress configurations. We discuss the dependence of solid volume fraction on shear rate under the constant pressure condition, and Bagnold scaling in volume controlled experiments. In addition, we study the influence of oscillatory driving on the system properties.

I. INTRODUCTION

A significant understanding of granular flow results from experimental measurements and numerical simulations. Simulations have proved to effectively complement the experimental measurements. Among many known advantages of computer simulations in any field of physics we can distinguish the following three types: 1) The ability to study the regions of parameter phase space that are difficult to access in experiment. For example, regarding granular experiments, high-frequency and/or high amplitude driving can be easily simulated but is difficult to achieve in experiments because of considerable power required; 2) The ability to study the system under (often simplified) conditions that are not reachable or are very difficult to have in experiments. For example, 2D simulations as opposed to 3D experiments, periodic boundary conditions as opposed to solid walls boundaries, etc.; 3) The ability to obtain more complete and detailed information under the same or close to the same conditions as in an experimental study.

However, in the subfield of sheared granular flow, most of the known numerical studies exploit either the first or the second advantage of simulations from the above list.[2,3,4,5,6,7,8,9] In particular, there are very few efforts to model realistically the physical boundaries, and this is the most common discrepancy between the set-up of laboratory experiments and the set-up of numerical simulations. This effect of physical boundaries, such as the walls of the container, is often and rightfully considered responsible for the discrepancy between the results of the experiments and of the simulations, or between the predictions of the existing theories and the results of experiments or simulations.[10,11] Jenkins and Richman[12], for example, calculated boundary conditions in a specific limit for plane flow of identical, smooth, inelastic

disks interacting with a bumpy wall. Louge, Jenkins and Hopkins[13] and later Louge[14] tested these theoretical predictions for rapid sheared granular flows using computer simulations. The work of Nott, Alam, Agrawal, Jackson and Sundaresan *et al.*[11] presents the theoretical study of the effect of boundaries on the plane Couette flow, indicating the possibility of many different stable and unstable states of the flow, completely determined by the properties of the boundaries. However, to the best of our knowledge, none of the simulations reported in the literature for sheared granular flow are using the boundary models that closely reflect the geometry and the conditions of a Couette cell. Instead, simple models and boundary conditions are conventionally used to set and study sheared granular flow. Campbell and Brennen[3], for example, recognize the effect of shearing wall properties on velocity and granular temperature profile in 2D shearing cell by presenting in parallel the results for two models of particle-wall collisions: Type A model assumes the interaction between particles and the wall is similar to the interaction between particles and particles, and; Type B model attempts to approximate a no-slip condition by setting the after-rebounce velocity of a colliding particle equal to the velocity of the wall. Type B model has then been studied more extensively by many authors because it provides a constant shear rate and constant volume fraction throughout the sample and thus makes a convenient test case when comparison with theoretical predictions is considered. However, the experimental data indicate strongly the presence of boundary effects on the shear flow. The examples are the formation of a shear band, or other non-linear shear rate and volume fraction distributions in the sample (see e.g. Ref. 15), or the drastic difference between the shearing using a wall with glued particles on it as opposed to shearing the system by a plane frictional wall. Similarly, the periodic

boundary conditions, that are often used in simulations, neglect the effects of stationary walls on the shear flow.

In this paper we report the systematic study of the effect of boundary conditions on sheared granular flow in a Couette cell in zero gravity using event-driven simulations. The paper is organized as follows. Section II describes the numerical approach and relevant parameters of simulations. In Sec. III we present the results for bulk velocity and volume fraction profiles for the variety of boundary conditions, such as the system with rough shearing wall with and without glued particles on it. Also we consider simulations with oscillating bottom wall. We show the results for the systems of varied sizes, varied properties of the walls of a Couette cell, varied intensity of external driving, and discuss the effect of each varied parameter on the profiles and equilibrating times. In Sec. IV we discuss stresses on the physical boundaries of a Couette cell and their distributions. We compare the normal and shear component of the stress distributions and discuss the factors determining the widths of the distributions and their average values.

All the results in Secs. III A-IV are obtained for the systems of fixed or directly controlled total volume. In Sec. V we present the results for the stresses, velocities and volume fraction profiles for the systems with stress-controlled boundaries. We then discuss the differences between volume controlled and stress-controlled simulations. In particular, we consider the different response to the increase of the shearing velocity in these two configurations.

II. SIMULATION DETAILS

Numerical algorithm of our choice, event-driven algorithm for hard spheres, is well described elsewhere, for example in Ref. 16. In zero gravity all particles follow linear trajectories between the collisions. All collisions between particles are instantaneous and binary. Consider two colliding particles with diameter σ_1 and σ_2, masses m_1 and m_2, positions $\mathbf{r}_1$ and $\mathbf{r}_2$, linear and angular velocities $\mathbf{v}_1$, ω_1 and $\mathbf{v}_2$, ω_2. Then velocities after collision are:

$$\mathbf{v}_1' = \mathbf{v}_1 - \frac{m_2}{m_1 + m_2}\Delta\mathbf{V}; \ \mathbf{v}_2' = \mathbf{v}_2 + \frac{m_1}{m_1 + m_2}\Delta\mathbf{V} \quad (1)$$

$$\omega_1' = \omega_1 + \frac{m_2}{m_1 + m_2}\frac{\Delta\mathbf{W}}{\sigma_1}; \ \omega_2' = \omega_2 + \frac{m_1}{m_1 + m_2}\frac{\Delta\mathbf{W}}{\sigma_2} \quad (2)$$

where

$$\Delta\mathbf{V} = (1+e)\mathbf{v}_n + \frac{2}{7}(1+\beta)\mathbf{v}_t; \ \Delta\mathbf{W} = \frac{10}{7}(1+\beta)\left[\mathbf{n}\times\mathbf{v}_t\right] \quad (3)$$

Here $\mathbf{n} = (\mathbf{r}_2 - \mathbf{r}_1)/|\mathbf{r}_2 - \mathbf{r}_1|$ is the normal unit vector, $\mathbf{v}_n$ and $\mathbf{v}_t$ are the normal and tangential components of the relative velocity $\mathbf{v}_c = \mathbf{v}_1 - \mathbf{v}_2 - [(\frac{1}{2}\sigma_1\,\omega_1 + \frac{1}{2}\sigma_2\,\omega_2)\times\mathbf{n}]$ of particles at the contact point. Total linear and angular momentum are conserved during a collision, however, total translational and rotational energies are lost.

Energy dissipation is controlled by three parameters:[17] the coefficient of restitution e, coefficient of friction μ, and coefficient of tangential restitution β. The algorithm is adapted to include the particle's interaction with physical boundaries in the following way. The collisions between particles and the top or bottom walls (also called horizontal walls) assume that the wall is a particle of infinite radius, infinite mass, and of linear velocity equal to the wall's velocity at the point of contact. Three dissipation parameters, e_w μ_w and β_w, characterize these collisions. In the collisions between free and glued (to be explained below) particles we use the same dissipation parameters as in the collisions between free particles. In the calculation of the re-bounce velocity we assume that a participating glued particle has an infinite mass. Finally, the side walls are the particles of infinite mass and of infinite radius and with the surface normal at the point of contact pointing horizontally toward the center of the cell. The properties of the side-walls are characterized by the separate set of dissipation parameters, e_s, μ_s and β_s.

Experiments and theoretical studies show that the coefficient of restitution e noticeably depends on the impact velocity.[18,19] To account for this effect, we set this coefficient for all types of collisions to be velocity dependent in a way suggested in Ref. 20

$$e(v_n) = \begin{cases} 1 - Bv_n^{3/4}, & v_n < v_0 \\ \epsilon, & v_n > v_0 \end{cases} \quad (4)$$

Here v_n is the component of relative velocity along the line joining particle centers, $B = (1-\epsilon)v_0^{(-3/4)}$, $v_0 \simeq 100\,\langle d\rangle/sec\,\epsilon$ is a restitution parameter that characterizes the material properties of the particles or walls: Decreasing ϵ is equivalent to increasing the energy dissipated during each collision.

Coefficient of tangential restitution, β, defined as the ratio of the tangential components of the relative velocity after and before collision, is assumed to be the one suggested in Ref. 21 and used in Ref. 20, i.e.

$$\beta = \begin{cases} -1 + \mu(1+e)(7/2)v_n/v_t, & \text{for sliding contacts} \\ \beta_0, & \text{for rolling contacts} \end{cases} \quad (5)$$

Here μ is the coefficient of friction, e is given by (4), and β_0 is a parameter which also has a meaning of restitution of velocity in the tangential direction for sliding contacts. As in Ref. 21, the choice between rolling and sliding solution depends on the ratio of normal to tangential component of relative velocity, and on the parameters β_0, ϵ, μ. The same functional dependence is assumed for β_w, e_w, and for β_s, e_s.

Table I summarizes our choice of dissipation parameters for typical configurations. When different dissipation parameters are used in the simulations, the results are always compared to the typical configuration.

We have carried out the simulations using a 3D granular system of polydisperse inelastic frictional spheres in the Couette cell, Fig. 1, with stationary side walls, ro-

TABLE I: Typical choice of dissipation parameters.

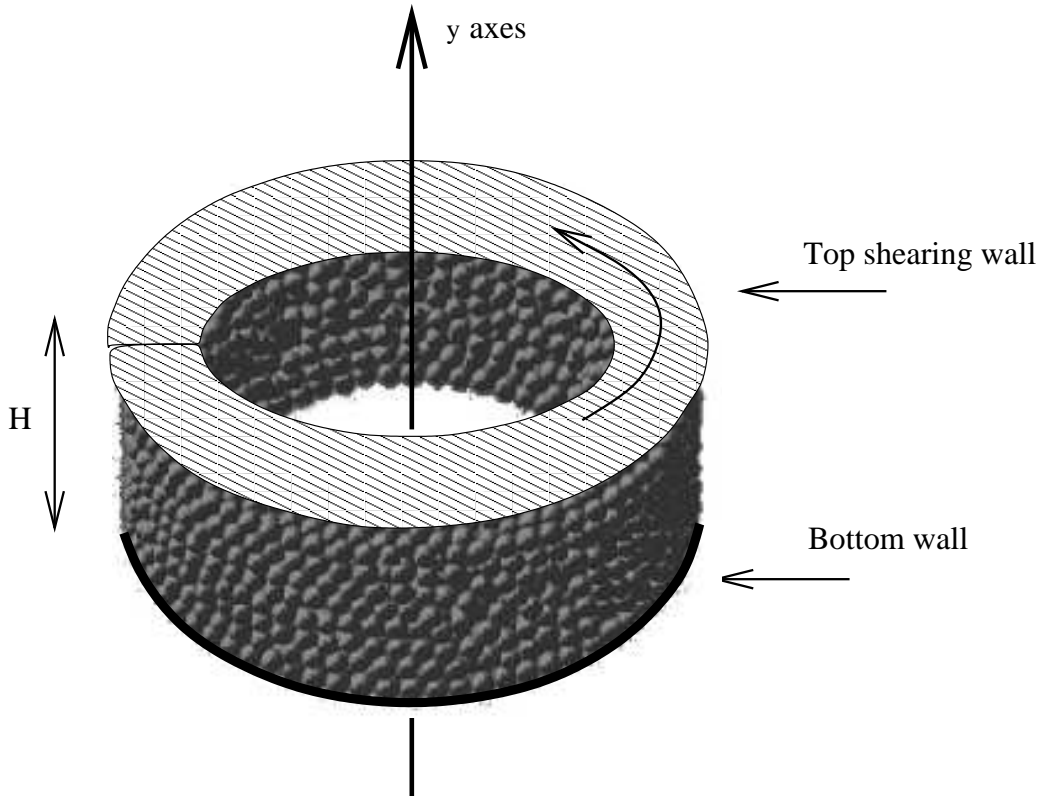| particles (including glued)	$\epsilon = 0.6$	$\mu = 0.5$	$\beta_0 = 0.35$	frictional inelastic particles
top and bottom walls	$\epsilon_w = 0.1$	$\mu_w = 0.9$	$\beta_{0w} = 0.35$	very frictional and inelastic
side-walls	$\epsilon_s = 0.9$	$\mu_s = 0.1$	$\beta_{0s} = 0.35$	slightly frictional and inelastic

FIG. 1: Granular matter between two concentric stationary cylinders - side walls (not shown in the figure). Top wall is rotating around the vertical y axes. Bottom wall can be vibrated in the vertical direction in volume controlled simulations, or it can move in the vertical direction in stress controlled simulations.

tated top wall, and the bottom wall that can move in the vertical direction.

The last feature allows us to oscillate the bottom wall. The motivation for these oscillations is that they are often used in laboratory experiments performed with granular systems of high volume fraction in order to fluidize otherwise jammed state[22]. We use the oscillating bottom wall to study the effect of oscillations on the granular flow and to make the connection with the laboratory experiments, where possible.

In addition, the moving bottom wall feature is actively used in stress controlled simulations, where we allow granular particles to determine the position and the velocity of the bottom wall on their own. Here the stress constraint determines the average volume fraction. We refer to Section V for more detailed discussion of this configuration.

The particles are polydisperse with diameter values randomly distributed in the range $[0.9, 1.1]\ \langle d \rangle$, where

$\langle d \rangle$ is the average diameter of particles, that is used as a natural length scale. Our *typical configuration* consist of $N = 2000$ particles, and fixed radii of inner cylinder and outer cylinder ($R_i = 8\langle d \rangle$, $R_o = 12\langle d \rangle$). The height H of the Couette cell is variable and in general is a function of time and preset average total volume fraction ν for the volume controlled simulations, and it is the function of time and preset average stress on the bottom wall in stress controlled simulations. In the case of volume controlled simulations we have

$$H(\nu, t) = \left(4.22\frac{1}{\nu} + A\sin(\omega t)\right)\langle d \rangle. \qquad (6)$$

Here A, ω are the amplitude scaled by $\langle d \rangle$, and the frequency in rad/sec of the bottom wall vibrations, if any. Thus, in absence of vibrations, $H = 10.54\langle d \rangle$ for $\nu = 40\%$; $H = 21.10\langle d \rangle$ for $\nu = 20\%$ and $H = 8.44\langle d \rangle$ for $\nu = 50\%$. Our typical choices for the amplitude and frequency of the vibrations of the bottom wall are $A = 1\langle d \rangle$

and $\omega_t = 230\,rad/sec$ or $f = \omega_t/2\pi = 36.6\,Hz$. These amplitude and frequency set the dimensionless parameter $\Gamma = A\omega^2/g$ to the value which is above critical for the onset of fluidization, $\Gamma = 5 > \Gamma_c = 1$. We use the value of gravitational constant $g = 9810\langle d\rangle/sec^2$ ($= 981\,cm/sec^2$ when $\langle d\rangle = 0.1\,cm$).

Another system size studied in this work is a *wide configuration* that has $N = 5000$ particles in a Couette cell with radii of inner and outer cylinders $R_i = 5\langle d\rangle$ and $R_o = 15\langle d\rangle$, respectively, and H given by (6).

We assume the surface properties of side walls to be the same for inner and outer cylinder and different from the properties of top and bottom walls. The top wall can be covered with particles glued to its surface. These glued particles have the same polydispersity, mean diameter and material properties as the free particles. They are glued into the dimples on the surface so that each one protrudes inside the cell by the distance of half it's diameter. Figure 2 shows a typical distribution of glued particles on the inside surface of the top wall. For both typical and wide configurations the number of glued particles corresponds to $\approx 30\%$ surface fraction.

III. VELOCITY AND VOLUME FRACTION PROFILES

To measure velocity and volume fraction profiles, the volume of Couette cell is divided in N_s ring slices, Fig. 3 (a). Each slice is assigned a y bin number $i_y = 1, ..., N_s$. In most cases, we set $N_s = 10$ and the height of one ring slice is $h_y = 1.05\langle d\rangle$. When the bottom wall is oscillated, we account for variable volume of the bottom slice or slices. In our measurements we average a studied quantity both over the volume of a y bin and over the time interval t_p, typically $t_p = 0.5\,sec$. Within this time interval we measure the particle's velocities and volume fractions periodically every δt_p leading to $N_p = t_p/\delta t_p$ different distributions. It is convenient to express times in terms of the following time scale

$$T_w = \frac{2\pi}{\omega_t} \qquad (7)$$

Time T_w correspond to the period of oscillation with frequency ω_t. Thus $t_p = 18.3\,T_w$, and we use $\delta t_p = T_w/10$. T_w is used as a scale independently of whether the system is vibrated or not. All particles are binned in the corresponding ring slices, and the average solid volume fraction and the average tangential velocity in each bin are calculated as a function of y bin number.

For wide configurations, in addition we measure the volume fraction as a function of the distance to the inner cylinder. In this case the volume of Couette cell is divided into a set of vertical shells as in Fig. 3(b). Each shell is assigned r bin number. The averaging procedure is analogous to the one described above for y profiles.

In the figures of this paper, the steady state velocity profiles are shown as lines with filled triangles. The "shadow of broken lines" below the steady state velocity profile are transient state velocity profiles measured periodically - typically every 1/12 of the total simulation time. Filled circles mark the steady state volume fraction profiles. Transient states for volume fraction are also shown as the collection of broken lines. For each case we show the scaled energy plot as a function of time. The scaled energy is measured kinetic energy per particle scaled by the energy of a particle of average diameter and of average linear top wall velocity. These energy plots allow to determine whether and when the system reaches a steady state.

A. Typical configurations with inelastic and frictional sidewalls

Figure 4 shows the velocity profiles, top horizontal panel, scaled total kinetic energy, second horizontal panel, and average size of particles $\langle d\rangle$, third horizontal panel. All the measurements are done for the typical configuration systems with 2000 particles and in zero gravity, but with four different boundary conditions. The first column of graphs, (a), shows the results for the system with oscillating base and glued particles on the top wall. The second column, (b), shows the results for the system with oscillating bottom wall but without glued particles. The last two columns show the results for the system without oscillating bottom wall with (c) and without (d) glued particles. When oscillations are present, the vertical y coordinate of the bottom wall is given by $y = Asin(\omega t)$, with amplitude $A = \langle d\rangle$ and frequency $\omega = \omega_t = 230\,rad/sec$.

In all four cases the shearing wall is rotating with 10 rad/sec. This sets the linear shearing velocity range between 80 $\langle d\rangle$/sec (close to inner cylinder) and 120 $\langle d\rangle$/sec (close to outer cylinder). The effect of different shearing velocities is discussed in Sec. III C and also later in Sec V A.

First we consider results without oscillations. Figure 4(a) shows that in the case of glued particles on the top wall, the system reaches a state characterized by a significant shear throughout the domain. By comparing 4(a) and 4(b), we see that there is clearly a strong effect of glued particles on increasing shear throughout the domain. We emphasize that the top wall without glued particles, Fig. 4(b), does not lead to significant shear, although the wall itself is very frictional and inelastic, see Table I.

Figure 4(c-d) shows the results with oscillations. The addition of oscillations accounts for a considerable slip velocity at the bottom wall. Similarly to the case without oscillations, the presence of glued particles greatly reduces the slip velocity at the top wall. Oscillations are also accountable for size segregation: The first two bins in cases (c) and (d) are populated mostly by small diameter particles, as it can be seen in the bottom panel. We also note (Fig. 4, top panel) a very small volume fraction
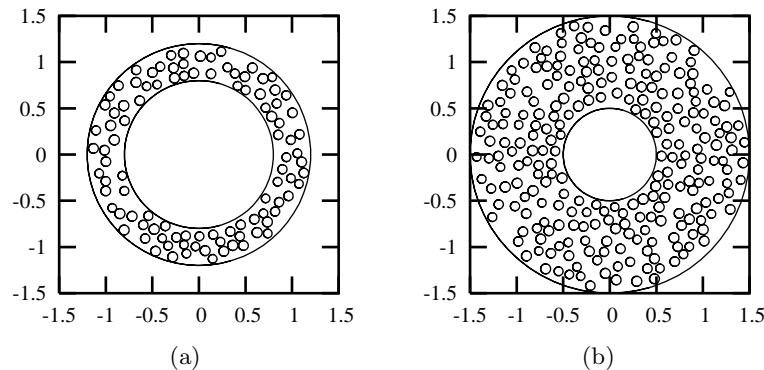
FIG. 2: (a) Typical configuration: distribution of 100 glued particles on a shearing surface, surface volume fraction $\approx$ 30%; (b) Wide configuration: distribution of 250 glued particles, surface volume fraction $\approx$ 30%.
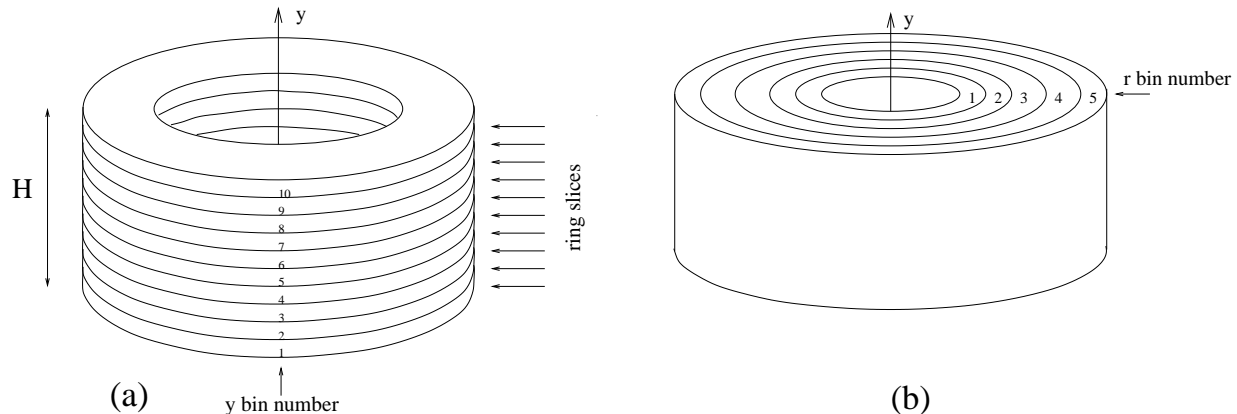

FIG. 3: (a) y bin number in measurements of velocity and volume fraction profiles. (b) r bin number for wide configurations.

close to the bottom wall. This is due to the fact that when the bottom wall moves downward, the adjacent granular layer does not follow it, except possibly small diameter particles. This observation is also confirmed by computer visualization of the granular layer.

The distribution of volume fraction as a function of y is shown on the same plots as velocity distribution. The steady states, marked by filled circles, show that the volume fraction is not uniform. For each of four cases we observe the maximum local volume fraction $\approx$ 58% for some intermediate y's, with dilation effects close to the walls, in particular the top one.

From energy plots we estimate the equilibrating time for all four cases: $t_{eq}(a) = 15\,sec$, $t_{eq}(b) = 15\,sec$, $t_{eq}(c) = 2\,sec$, $t_{eq}(d) = 6\,sec$. These times are shorter for the systems with oscillating bottom wall, due to increased collision rate. Also, oscillations lead to modulation of the scaled energy; this is shown in the insets in the energy plots. In addition, in the systems with oscillations, the glued particles provide an increase in collision rate and decrease in equilibration time; their effect on equilibrating time is weak in the system without oscillations.

B. Wide configurations with inelastic and frictional sidewalls

Next, we consider the velocity and volume fraction profiles for wide configuration, characterized by 5000 particles, and 40% solid volume fraction, using typical values of all other parameters. The results for the same four boundary conditions as above are shown in Fig. 5.

The top panel shows the velocity and volume fraction profiles. Qualitatively these results are similar to the results for typical configuration shown in Fig. 4 (top panel), although there are some differences. For example, we see that the velocities are larger for wide configurations. This can be explained by realizing that the ratio of the areas of dissipative sidewalls to the area of shearing wall is smaller. Therefore, the influence of side walls is weaker in wide configuration compared to typical configuration. This effect also leads to larger slip velocity at the bottom wall. On the other hand, the volume fraction profiles are very similar in these two configurations.

The second panel of Fig. 5 shows the velocity profiles averaged over cylindrical shells of increased radius [see Fig. 3(b)]. To obtain these results we split the volume of the cell into five concentric cylindrical shells of same
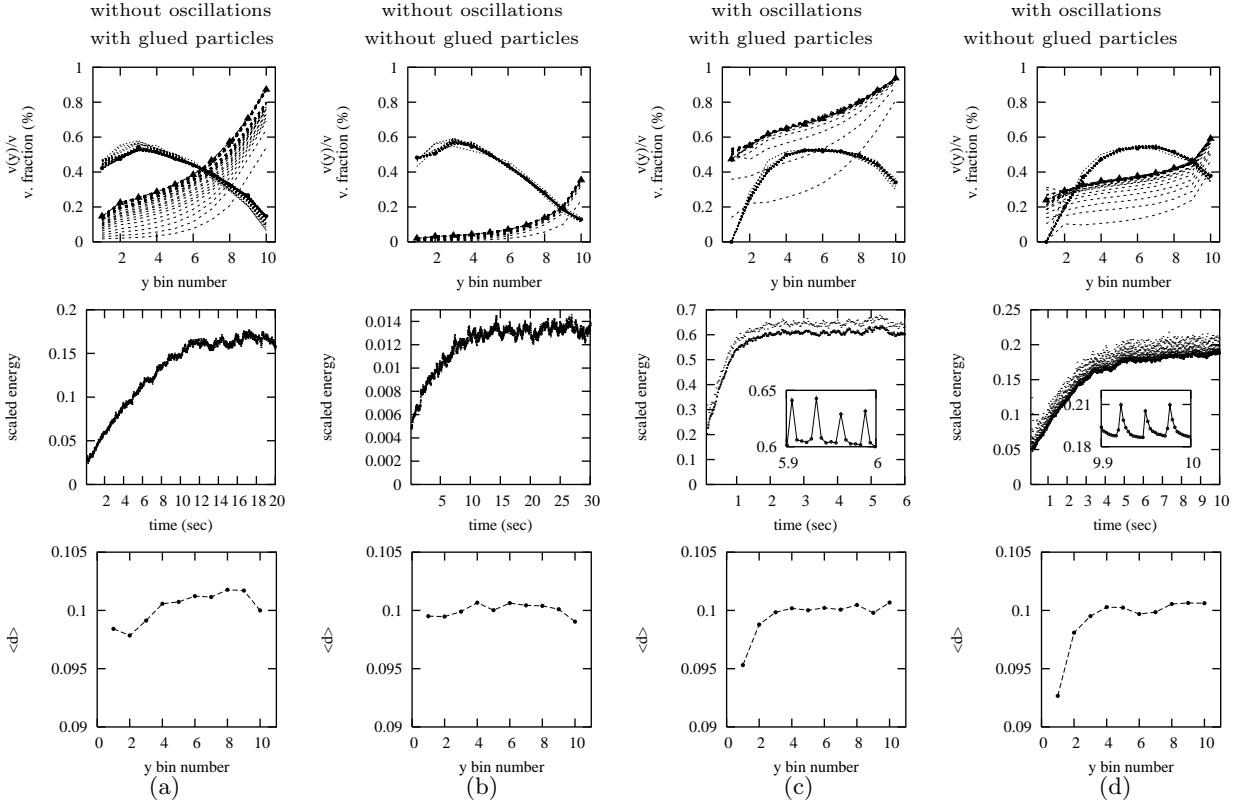
FIG. 4: Typical configurations results. First Panel: scaled velocity profiles (filled triangles) and volume fraction profiles (filled circles) in steady state regime together with the profiles in transient regimes (dashed lines). Second panel: scaled energy plots. Insets in energy plots: kinetic energy plotted on a shorter time scale showing the frequency of bottom wall oscillations. Third panel: average diameter of particles. (a), (b) - results without oscillating bottom wall; (c), (d) - with oscillations; (a), (c) - shearing wall with 100 glued particles; (b), (d) - without glued particles. In all simulations the dissipation parameters are as shown in Table I.

thickness. Each shell is given a number 1 to 5 with higher number corresponding to the larger radius: The profiles for shell 1 are not shown since the reduced volume fraction near inner cylinder (see the third panel of Fig. 5) does not allow for good statistics. For comparison, the results for the velocity averaged over the whole volume are also replotted as solid lines. These results indicate that, as we change the location of the averaging shell inside the cell, the changes of the velocity profiles shape are small, if not negligible. We note here that these results are obtained assuming side walls are characterized by relatively small friction and dissipation. Therefore, there is no observable slow-down of the particles in the vicinity of the side walls.

Figure 5, third panel, shows the radial volume fraction distribution obtained from averaging the volume fraction in each cylindrical shell. As in the case of volume fraction profiles in the vertical direction, the dashed lines mark the transient states and the solid lines with filled circles mark the steady state distributions. We observe significant dilation near the inner wall. This is due to centrifugal effect: Particles colliding with the top wall gain the momentum that, on average, has a direction along the tangent line to the trajectory at the contact point.

Following this direction, particles get closer to the outer wall. When shearing is strong, as in the cases (a), (c), and (d), we also observe dilation band close to this wall.

Finally, Fig. 5, forth panel, shows the scaled energies obtained similarly to the results in Fig. 4 (third panel), but averaged over longer time periods to reduce noise (therefore, called "mean"). Comparing energy plots in Figs. 5 and 4 we see similar estimates of the equilibrating times for all the boundary conditions, except the one without oscillations and without glued particles. Here we notice huge increase of equilibrating time. An explanation for this increase is that the time period to establish steady radial volume fraction distribution is very long, as illustrated in Fig 5(b), third panel.

C. Effect of dissipation parameters and shearing velocity in the systems without oscillations

Next, we discuss system's behavior when we modify the dissipation or the driving parameters. As a basis, we use the 40% volume fraction typical configuration system without oscillations and without glued particles, Fig. 4(b), with one modification: to enhance the shearing
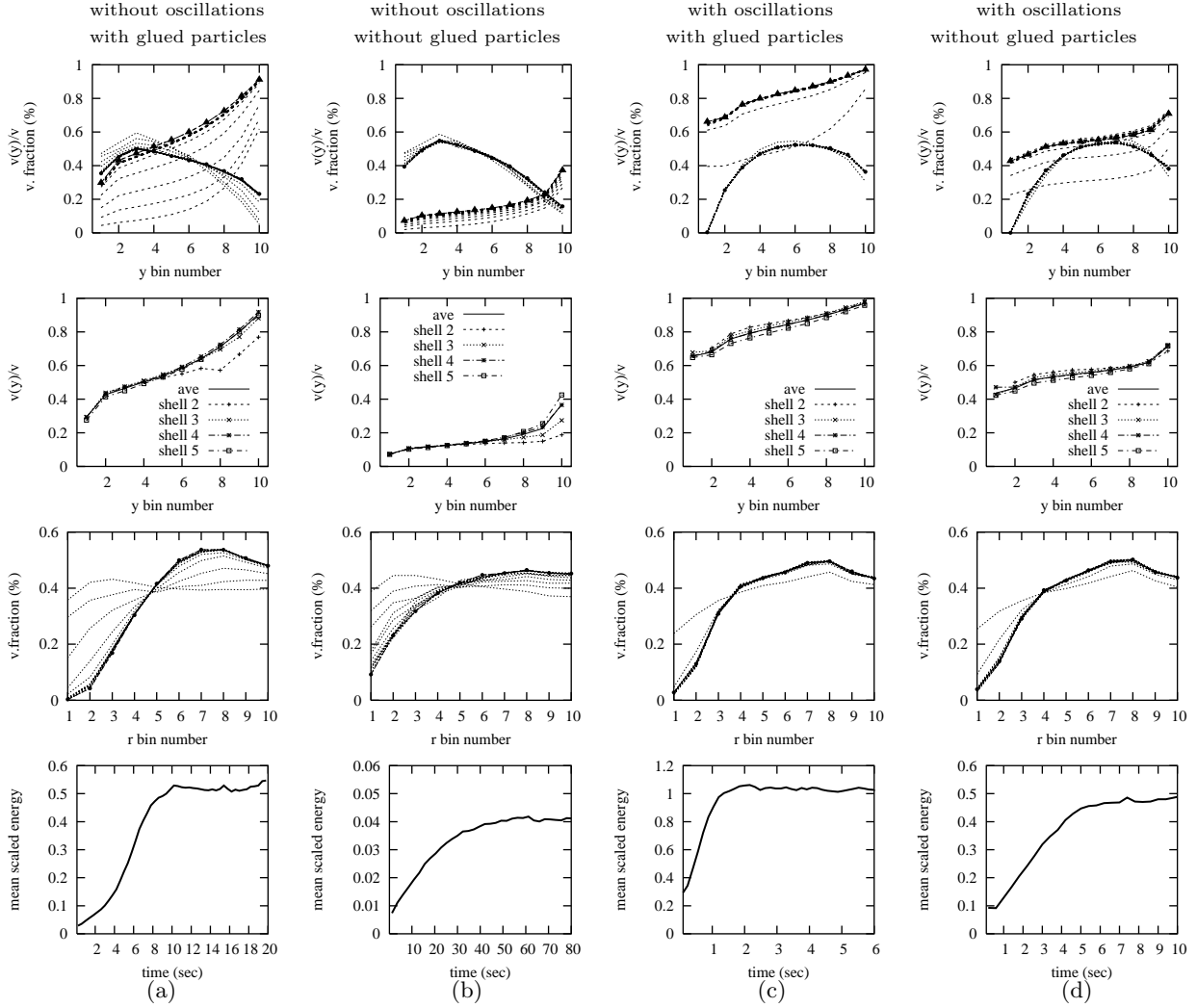
FIG. 5: Results for wide configurations. First Panel: scaled velocity profiles (filled triangles) and volume fraction profiles (filled circles) in steady state regime together with the profiles in transient regimes (dashed lines). Second panel: velocity profiles measured in cylindrical shells (as discussed in the text) scaled by shell's shearing velocity. Third panel: radial volume fraction profiles. Forth panel: scaled energy plots. As in Fig. 4, (a) and (b) are without oscillations, (c) and (d) are with oscillations, (a) and (c) are with glued particles on a top wall, and (b) and (d) are without glued particles.

throughout domain, we replace the dissipative side walls by completely elastic side walls.

There is a significant, qualitative difference of the velocity profiles for the system with elastic and smooth side walls shown in Fig. 6 compared to inelastic and rough sidewalls shown in Fig. 4(b). Effect of shearing is much stronger in the systems with elastic side walls. In this case, the velocity profile is almost linear with very large slippage velocity at the bottom wall, and almost no slippage at the top wall. We refer to this shape of velocity profile as *linear-asymmetric*. The asymmetry is the history related effect: If we shear the same initial configuration by rotating the top wall in one direction and bottom wall in the opposite one, but with the same magnitude of velocity $V/2$, we obtain *linear-symmetric* velocity profile with equal slippage velocity at the top and bottom.

Figure 6 shows that the velocity and volume fraction

profiles are very similar as shearing velocities are varied. Additional simulations have shown that the velocity and volume fraction profiles are almost identical for all the tested values of V between 0.1 rad/sec and 35 rad/sec. The energy plots (bottom panel in Fig. 6) show, however, that the time to reach the steady state (*equilibrating time*), t_e, does depend strongly on V. This effect is shown in more detail in Fig. 7, which shows that t_e is inversely proportional to V. Therefore the same amount of strain is needed to reach the steady state for all explored shearing velocities.

In the next set of simulations we investigate the effect of horizontal walls properties in the same system. Out of three parameters that characterize the properties of horizontal walls, see Table I, we vary one at a time and keep the others fixed. Table II summarizes our findings by describing the shearing regime for the selected ranges
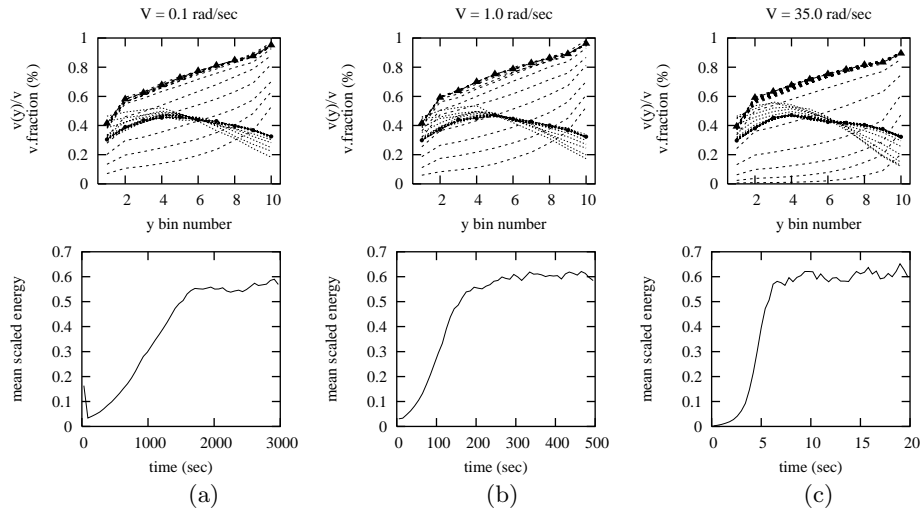
FIG. 6: Linear-asymmetric velocity profiles for the case of elastic sidewalls, no glued particles, and no oscillations. Shearing velocity is (a) $V = 0.1$ rad/sec, (b) $V = 1.0$ rad/sec and (c) $V = 35$ rad/sec.
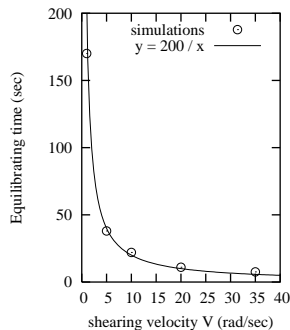

FIG. 7: Equilibrating times t_e in simulations (open circles) are evaluated from corresponding scaled energy plots and plotted against shearing velocity (elastic side walls, no glued particles, and no oscillations).

of the varied parameter.

We find that ϵ_w and β_{0w} have relatively weak effect on the velocity profiles. However, the coefficient of friction, μ_w, influences the flow strongly. There exists a critical value μ_w^c, below which the frictional force from the shearing wall cannot excite the granular flow. For our configuration this value is $\mu_w^c <\approx 0.4$, for the tested range of V's. In what follows, we explain the influence of μ_w on these profiles in some more detail.

Figure 8 shows the results for μ_w in the interval $[0.4, 0.9]$. Here, we observe that the systems first reaches a metastable state of slow shearing [open symbols in Fig. 8 (a) and (b)]. This metastable state is characterized by negligibly small slippage velocity at the bottom wall and very large slippage at the top, as well as by high volume fraction close to the bottom wall. As time progresses, the shear of the granular particles is increasing very slowly. However, after certain time the system jumps into a stable state of fast shearing with asymmetric-linear profile, also shown in Fig. 8 (a) and (b). We call this behavior *delayed dynamics*. Figure 8(c)

shows the scaled energy plots for four values of friction which illustrate this jump from metastable to stable state.

Figure 8(d) shows the crossover *transition time*, t_c. This transition time t_c (obtained in the manner discussed below) is defined as the time when metastable state ends, *i.e.* when the granular layer starts to pick up the energy fast. We find that the inverse square function $t_c = a/(\mu_w - \mu_w^c)^2$ is a good representation of the dependence of t_c on μ_w; this fit is also shown in Fig. 8(d). The critical friction for the onset of shearing μ_w^c is now the fitting parameter of the function. Using a fitting routine, we obtain $\mu_w^c = 0.33$.

Figure 9 illustrates the manner in which t_c is obtained. This figure shows scaled energies with the tangent lines (shown as skewed broken lines) at the points where the energy increase rate is maximum. The intersection of this tangent line and the time axis gives an estimate of t_c, and the intersection of the tangent line and the horizontal line at the level of the average scaled energy in the steady state gives an estimate of equilibrating time, t_e. In all

TABLE II: Shearing regimes for different horizontal walls properties.

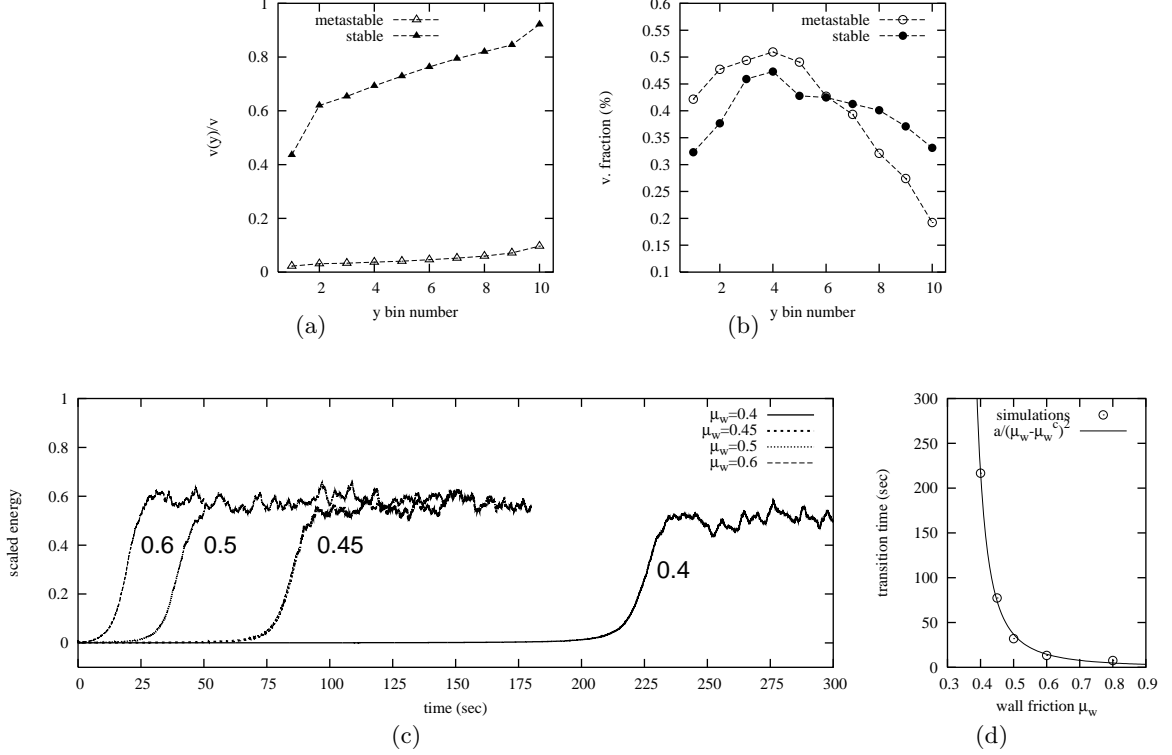| normal restitution	tang. restitution	friction	
ϵ_w [0.6-0.9]	β_{0w} [0.0-0.9]	μ_w [0.0-0.33]	μ_w [0.33-0.9]
linear-asymmetric	linear-asymmetric	no shearing	linear-asymmetric

(a)

(b)

(c)

(d)

FIG. 8: Delayed dynamics regime. The shearing velocity in all cases is $V = 10$ rad/sec. (a) and (b) show the typical velocity and volume fraction profiles in metastable and stable states, using $\mu_w = 0.45$ at $t = 30\,sec$ (metastable state) and $t = 150\,sec$ (stable state). (c) Scaled energy as a function of time for four values of μ_w. (d) Transition times, t_c, versus friction: open circles are the simulation results, and the solid line is the best fit using inverse function $t = a/(\mu - \mu_c)^2$ with fitting parameters $a = 1.07$ and $\mu_w^c = 0.33$.
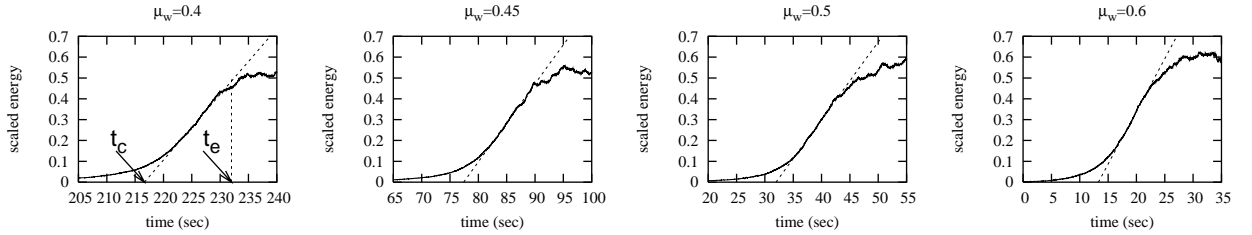

FIG. 9: Close-up of "transition interval" allows to determine the *transition time* t_c and equilibrating time t_e, as discussed in the text.

four cases, shown in Fig. 9, $\delta t_e = t_e - t_c$ is approximately (18 ± 4) sec. This result is consistent with the result for equilibrating time for the same $V = 10\,rad/sec$ and for high friction horizontal walls ($\mu_w = 0.9$), shown in Fig. 7. For such a large μ_w, $t_c \approx 0$, and $\delta t_e \approx t_e$.

Next, we consider influence of shearing velocity for fixed friction coefficient $\mu_w = 0.45$. Figure 10(a) shows

the scaled energy in the transition time interval for the system in delayed dynamics regime for three different shearing velocities, $V = 5\,rad/sec$, $V = 10\,rad/sec$, and $V = 20\,rad/sec$. This figure confirms that the transition times t_c depend very weakly on V. They are all slightly scattered around the value $t_c \approx 80\,sec$. However, the δt_e's are following the inverse rule shown in Fig. 7 (note
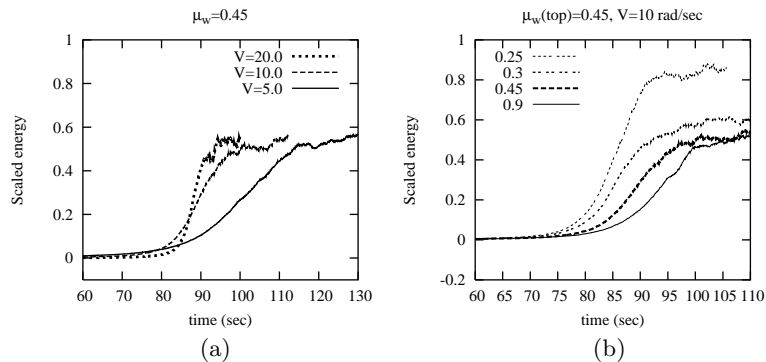
FIG. 10: Scaled energies in the transition interval for (a) $\mu_w = 0.45$ with three different shearing velocities, (b) $\mu_w = 0.45$ fixed for the top wall, variable μ_w for the bottom wall, fixed shearing velocity $V = 10\,rad/sec$.

that $t_c = 0$ for $\mu_w = 0.9$ used in Fig. 7). Therefore, δt_e's strongly depend on the shearing velocity, while being almost independent of the coefficient of friction.

To understand precisely the role which the horizontal walls play in the mechanism of delayed dynamics, we have performed simulations with fixed coefficient of friction of the top wall $\mu_w(top) = 0.45$ and varied coefficient of friction of the bottom wall. The results, shown in Fig. 10(b), clearly indicate that $\mu_w(bottom)$ does not have the determining effect on the transition time t_c. For example, changing it from 0.9 to 0.25 leads to less then 5% decrease of t_c. However, the higher slope of energy increase for smaller friction coefficients leads to smaller δt_e. We also note that for these low $\mu_w(bottom)$ the energies are rising to the higher values. This is an indication of higher overall velocities of the particles in the steady state due to higher slippage at the bottom wall for lower $\mu_w(bottom)$.

Based on the results shown in Figs. 7-10, the mechanism of the delayed dynamics can be explained as follows. The friction of the top wall controls the amount of the tangential momentum given to the particles colliding with it. Thus the energy input to the granular system is determined by the top wall friction, as well as by the collision rate of the particles with this wall. When the initial configuration is subjected to shear, the particles immediately dilate close to the top wall and form the cluster of high volume fraction close to the bottom wall. Reduced number of particles close to the top wall then significantly decreases the input of energy. If the friction of the top wall is low enough, below some critical value μ_w^c, all the energy is quickly dissipated without inducing shear in the system. For higher frictions, the energy transfered to the granular system starts to accumulate slowly: The shearing throughout the sample increases, until, at some critical time t_c, the shearing between the dense cluster and the bottom wall is big enough to dilate a region next to this wall and to push the cluster closer to the top wall. This process is sped up if $\mu_w(bottom)$ is smaller. As a result, the collision rate with the top wall increases, and the energy from this wall is rapidly

transfered into the kinetic energy of the whole cluster, until the stable state characterized by linear asymmetric profile forms. Thus, the time span of metastable state t_c is determined mostly by the friction of the top wall, and the time δt_e is determined mostly by the shearing velocity.

D. Effects of oscillations

To test the effect of the amplitude A and frequency f of oscillations, it is more convenient to go back to typical dissipative sidewalls used in Sec. III A. The reason is that in the case of smooth side walls the slippage velocity at the bottom wall is approaching the value of shearing velocity (this is shown later in this Section), making the analysis of the velocity profiles difficult. So, as a base system we use the "oscillating bottom wall, no glued particles" configuration shown in Fig. 4(d).

Figure 11 shows the results for velocity, volume fraction and equilibrating times for the systems where: (a, b) f is fixed and A is varied, (c, d) A is fixed and f is varied. The characteristic feature of the systems shown in Fig. 11 is the high volume fraction ($\nu \approx 50 - 60\,\%$) band of the granular layer in the middle of the cell height, confined between two thin layers of low ν close to the bottom and top walls. Inside this band the local shear rate is rather low, compared to the overall shear rate V/H. The highest local shear rates are observed only close to the top wall, while the high slippage velocities are observed at both top and bottom wall.

Figure 11(a) shows the amplitude dependence of the velocity and volume fraction profiles for fixed frequency $f = 36.6\,Hz$. We observe that the slippage of the bottom wall depends strongly on A, with higher A's leading to more slippage. Also, as A increases, the peak in the volume fraction profile moves further away from the oscillating wall. The equilibrating times, Fig. 11(b), decrease with an increase of A in a roughly linear manner.

Figure 11(c) shows the frequency dependence of the velocity and volume fraction profiles. Here, A is fixed
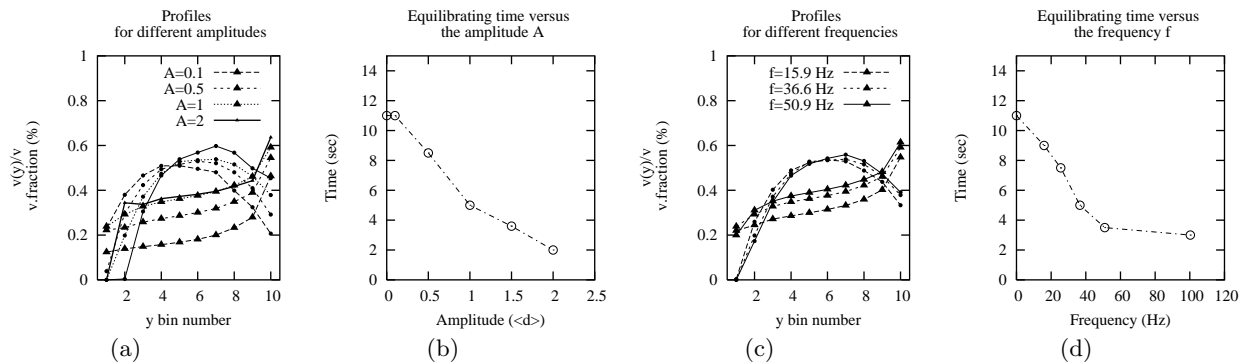
FIG. 11: Velocity and volume fraction profiles for (a) fixed frequency, $\omega = \omega_t$ ($f = 36.6\,Hz$), and different amplitudes of oscillations; (c) fixed amplitude, $A = \langle d \rangle$, and different frequencies. Also, equilibrating times are shown as a function of (b) amplitude and (d) frequency of oscillations. The volume fraction symbols follow the line pattern of the amplitude (a) or frequency (c) ones.

to $1\,\langle d \rangle$. The results show, again, that an increase of the intensity of oscillations, *i.e.* frequency, leads to an increase of velocity throughout the system. However, the volume fraction profiles change very little with f. The equilibrating times, Fig. 11(d), decrease with an increase of f, with the lower rate of decrease for higher f's.

Previously, by comparing Fig. 4(b) and Fig. 6, we saw significant effect of sidewall properties on velocity and density profiles for the systems without oscillations. Figure 12 shows the corresponding results as properties of the sidewalls are modified in the case of oscillating bottom wall, and absence of glued particles. To simplify the comparison, Fig. 12(a) shows again the result for the typical case, Fig. 4(d). Setting $\mu_s = 0$, $\epsilon_s = 1$ [Fig. 12(b)] makes almost all particles move with shearing velocity. Setting $\mu_s = 0.5$, $\epsilon_s = 0.6$ [Fig. 12(c)] creates already enough dissipation of energy to almost completely resist the shearing force: even oscillations cannot improve shearing when sidewalls are very frictional. Next we explore whether it is μ_s or ϵ_s that influence the velocity profiles. Therefore, in Fig. 12(d) we show profiles and scaled energy data for $\mu_s = 0.1$, $\epsilon_s = 0.6$. By comparing (a) and (d) we see that the elasticity of the side walls does not have the observable effect on the velocity profiles. Therefore, μ_s plays the crucial role, similarly as observed regarding μ_w in Sec. III C. The volume fraction profiles and equilibrating times, on the other hand, very weakly depend on the side wall properties.

IV. NORMAL AND SHEAR STRESSES ON THE BOUNDARIES

Stresses in granular systems have been the focus of many studies, because of their importance in a number of engineering designs. A significant part of these studies[23,24,25] deals with theoretical continuum models where stress is considered as a mean local quantity. Therefore, the validity of these models depends on the strength of stress fluctuations on the scale which defines

"locality". The knowledge of stress distributions becomes crucial here. There are many experimental, numerical, and theoretical studies of stress fluctuations,[26,27,28,29] however, these studies deal with high volume fraction of static or slowly sheared granular systems. In these dense systems the distribution of stresses is characterized by an exponential decay for large stresses. It is speculated[28] that the exponential tails in stress distributions are related to the presence of force chains in these systems. However, recently, Longhi, Easwar and Menon[30] reported the experimental evidence of exponential tails in stress distributions in rapidly flowing granular medium, *i.e.* in the system where it was unlikely to find force chains in the traditional "static" sense.

The results presented in this Section deal with the stress distributions at the physical boundaries of rapidly sheared granular systems that are not dense, *i.e.* 40% volume fraction. Before presenting these results we should note that in order to make maximum connection with existing experimental results and theories, we calculate the stresses in a manner that is very similar to experimental methods, ı.e. we also introduce in our simulations stress sensors on the boundaries (more details provided below). In the low volume fraction and/or rapid flow regime these sensors can report zero stress during some measuring intervals, see, for example, Ref. 30. Therefore, the total distribution of stresses must contain the distribution of *non-zero stresses* and a weighted delta function to account for *zero stresses*. In what follows we make a clear distinction between zero and non-zero stresses and extend all relevant theoretical arguments to account for the presence of zero stresses.

We present the results for the stresses on the boundaries for the typical configuration systems shown in Fig. 4. More detailed analysis will be given for the particular system without oscillations and with glued particles, Fig. 4(a). Of particular interest here are the distributions of normal and shear stresses on the top and bottom walls. To calculate these stresses we cover the respective boundaries with a grid of square *stress sensors*, as shown
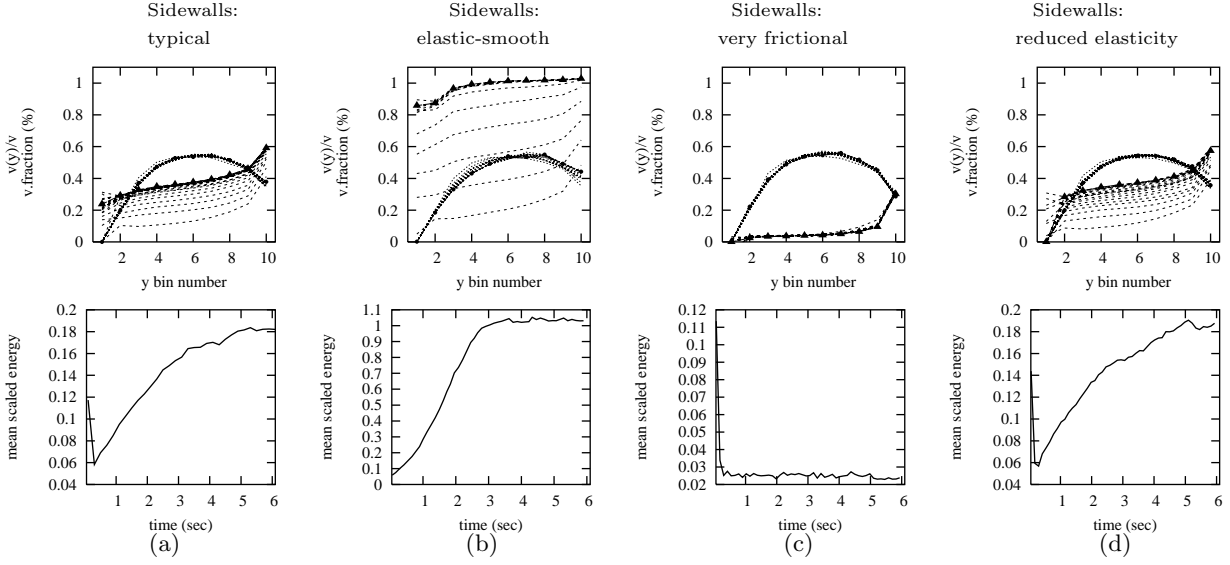
FIG. 12: Effect of sidewall properties on velocity and volume fraction profiles. (a) Base system, $\epsilon_s = 0.9$, $\mu_s = 0.1$, $\beta_{0s} = 0.35$. (b) Completely elastic and smooth. (c) $\epsilon_s = 0.6$, $\mu_s = 0.5$, $\beta_{0s} = 0.35$. (d) $\epsilon_s = 0.6$, $\mu_s = 0.1$, $\beta_{0s} = 0.35$.
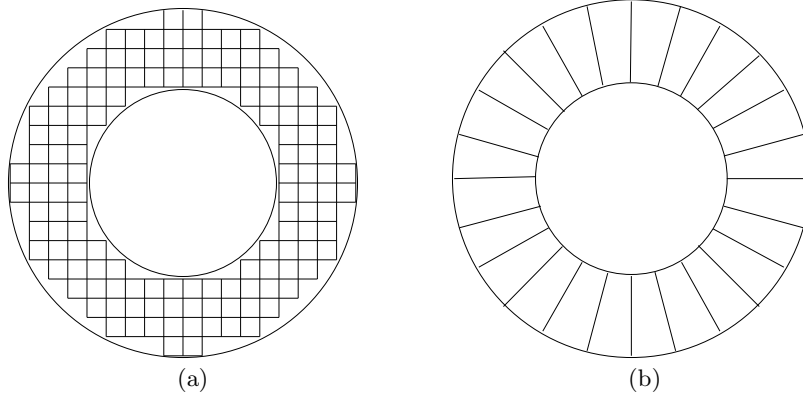

FIG. 13: Stress sensor areas between inner and outer cylinder of Couette cell. (a) Square sensors. Only the data from the sensors completely inside the volume of the cell are used. (b) Sector-shaped sensors.

in Fig. 13(a). All sensors have the same area $A_s = d_s^2$. Typically, we set $d_s = 1.09 \langle d \rangle$, $A_s = 1.19 \langle d \rangle^2$, and analyze the data only from the sensors that are completely inside the volume of the cell. Later in this Section we use *sector shaped* sensors, Fig. 13(b), which are convenient to set large sensor areas. The instantaneous normal and tangential stresses on a sensor are defined in the following way:

$$\sigma_n = \frac{\sum_i \Delta p_n(i)}{A_s \Delta t} = \frac{1}{A_s \Delta t} \frac{1}{6} \pi \rho_s \sum_i d_i^3 |v_y' - v_y| \quad (8)$$

$$\sigma_t = \frac{\sum_i \Delta p_t(i)}{A_s \Delta t} = \frac{1}{A_s \Delta t} \frac{1}{6} \pi \rho_s \sum_i d_i^3 (v_t' - v_t) \quad (9)$$

Here i counts all the collisions between the particles and the walls in the sensor area during a time interval Δt. We refer to this time interval as *averaging time*. $\Delta p_n(i)$ and $\Delta p_t(i)$ are the change of particle's normal and tangential components of momentum, ρ_s is the density of the solid material, d_i is the diameter of a particle participating in the collision i, and vectors $\mathbf{v}$ and $\mathbf{v}'$ are the velocities of the colliding particle before and after a collision, respectively. Subscripts n and t refer to the normal and tangential components. Our typical choice for the time interval is $\Delta t = T_w/10$. In order to get sufficient data for the stress Probability Distribution Function (PDF), we measure instantaneous stresses on all sensors every Δt for total of at least $\Delta T = 1000 \Delta t$. For the considered geometry, Fig. 13(a), we have the total of 124 sensors between the inner and outer wall. When presenting the results for stress distributions we show the scaled histograms (PDFs) of locally measured normal or tangential stresses, σ_n and σ_t, as a function of $\sigma_n/\langle \sigma_n \rangle$ or $\sigma_t/\langle \sigma_t \rangle$, respectively. The averages are defined as

$$\langle \sigma_{(n,t)} \rangle = (\sum_i \Delta p_{(n,t)}(i))/A_{base}/\Delta T \quad (10)$$

$$A_{base} = \pi(R_o^2 - R_i^2). \qquad (11)$$

Here i counts all collisions between the particles and the top or bottom wall during the whole measuring period $\Delta T = 1000\,\Delta t$.

A. Normal stress distributions

Figure 14 shows the results for normal *non-zero* stresses on the top and bottom walls in the typical configuration for the same four boundary conditions that were discussed in the preceding Section (see Fig. 4). The main features of the stress distributions are the increase from zero for small stresses and the decrease, in most cases approximately exponential, for large stresses. We note that it is well established experimentally that the exponential tails are the characteristic features of the stress PDFs in *static* granular materials at volume fractions close to the random close packing.[27,28,31] Although the stresses we measure are not static, nevertheless, the approximately exponential tails are observed in all cases shown in Fig. 14 (except perhaps for very large stresses). This is evident from the best fit of the following functional form

$$P_{nz}(\tilde{\sigma}) = c\tilde{\sigma}^n e^{-\tilde{\sigma}/\sigma_0}; \qquad \tilde{\sigma} = \sigma/\langle\sigma\rangle, \qquad (12)$$

shown in Fig. 14 as solid lines; we use $\langle\sigma\rangle = \langle\sigma_n\rangle$ as defined in (10). The subscript nz is used to emphasize that the distributions are build from non-zero stresses. This is important because certain fraction of sensors registers zero stress due to the fact that the volume fraction (typically 40%) is not sufficiently large to warranty that there is always a particle in contact with a sensor. Including zero stresses in the definition of P would prevent us from formulating the fitting function (12) and relate our results directly to experimental and theoretical results. We discuss the consequence of this approach in more details below.

Form (12) can be thought of as the generalization of the theoretical predictions for static stress distributions[42]. For example, the original q model proposed by Liu, Nagel, Schecter, Coppersmith, Majumdar, Narayan, and Witten[29,32] and extended later by other authors,[33,34] predicts the distribution (12) with $n = N_c - 1$, where N_c is the number of force transmitting contacts between a particle in one layer and particles in the adjacent layer. In three dimensions and *fcc* close packing $N_c = 3$, so $n = 2$. Using different approach, Edwards and Grinev[35] predict the distribution (12) with $n = 1/2$. n can also depend on the number of contacts between sensor and particles during averaging time, as will be shown in Sec. IV A 2. Therefore, it makes sense to think of n as a fitting parameter. Other parameters, c and σ_0, can be expressed in terms of n and the average stress $\langle\tilde{\sigma}\rangle_{nz}$ (measured directly in simulations) using the following expressions:

$$1 = \int_0^\infty P_{nz}(\tilde{\sigma})\,d\tilde{\sigma} = c\left[\Gamma(n+1)\sigma_0^{(1+n)}\right] \quad (13)$$

$$\langle\tilde{\sigma}\rangle_{nz} = \int_0^\infty \tilde{\sigma}P_{nz}(\tilde{\sigma})\,d\tilde{\sigma} = \sigma_0(n+1) \qquad (14)$$

In Fig. 14 we show the fit of the functional form (12) with n as the only fitting parameter. Other parameters, calculated using (13) and (14), and average quantities, obtained directly from simulations, are also shown. These results show that the average stresses $\langle\sigma\rangle$ (indicated in the horizontal axes labels on each plot) at the top and bottom walls are equal within the statistical error. However, the peak value and the width of a distribution is different in each case. In particular, for the systems without oscillations the distributions are wider at the top wall, while if oscillations are present, they are wider at the bottom wall. Before discussing this result, we first consider the effects of volume fraction, collision rate, averaging, and correlations on the properties of the stress distributions.

1. The width of stress distributions

In previous section we have shown that a distribution is determined by the parameter n and the average stresses $\langle\sigma\rangle_{nz}$ and $\langle\sigma\rangle$. Here we define the width of a distribution in terms of the above quantities and discuss its dependence on the various properties of granular system.

Let the width of a distribution be defined as the root mean square of all measured stresses (including zero stresses) divided by the mean stress

$$\text{width} = \frac{\sqrt{\langle\sigma^2\rangle - \langle\sigma\rangle^2}}{\langle\sigma\rangle} = \frac{\sqrt{\langle\tilde{\sigma}^2\rangle - \langle\tilde{\sigma}\rangle^2}}{\langle\tilde{\sigma}\rangle} = \sqrt{\langle\tilde{\sigma}^2\rangle - 1}$$
$$(15)$$

(here we use $\langle\tilde{\sigma}\rangle = 1$). The distribution itself takes the form of a linear combination of the distribution of non-zero stresses (12) and the delta function to account for zero stresses

$$P(\tilde{\sigma}) = C_1 P_{nz}(\tilde{\sigma}) + (1 - C_1)\,\delta(0) \qquad (16)$$

The constant C_1 signifies the fraction of non-zero stresses in the total distribution. Then, the mean and the mean square of the stress are as follows

$$\langle\tilde{\sigma}\rangle = \int_0^\infty \tilde{\sigma}P(\tilde{\sigma})\,d\tilde{\sigma} = C_1\langle\tilde{\sigma}\rangle_{nz} = 1 \qquad (17)$$

$$\langle\tilde{\sigma}^2\rangle = \int_0^\infty \tilde{\sigma}^2 P(\tilde{\sigma})\,d\tilde{\sigma} = C_1\sigma_0^2(n+1)(n+2) \quad (18)$$

From the first equation we obtain $C_1 = 1/\langle\tilde{\sigma}\rangle_{nz}$ and, using (14), we arrive at the following expression for the width of distribution:

$$\text{width} = \sqrt{\sigma_0(n+2) - 1} = \sqrt{\sigma_0 + \langle\tilde{\sigma}\rangle_{nz} - 1} \qquad (19)$$

Expression (19) reduces to the simple $\sqrt{\sigma_0} = (n+1)^{-1/2}$ in the case of *absence of zero stresses* when all sensor register at least one strike per Δt and $\langle\tilde{\sigma}\rangle_{nz} = \langle\tilde{\sigma}\rangle = 1$. In
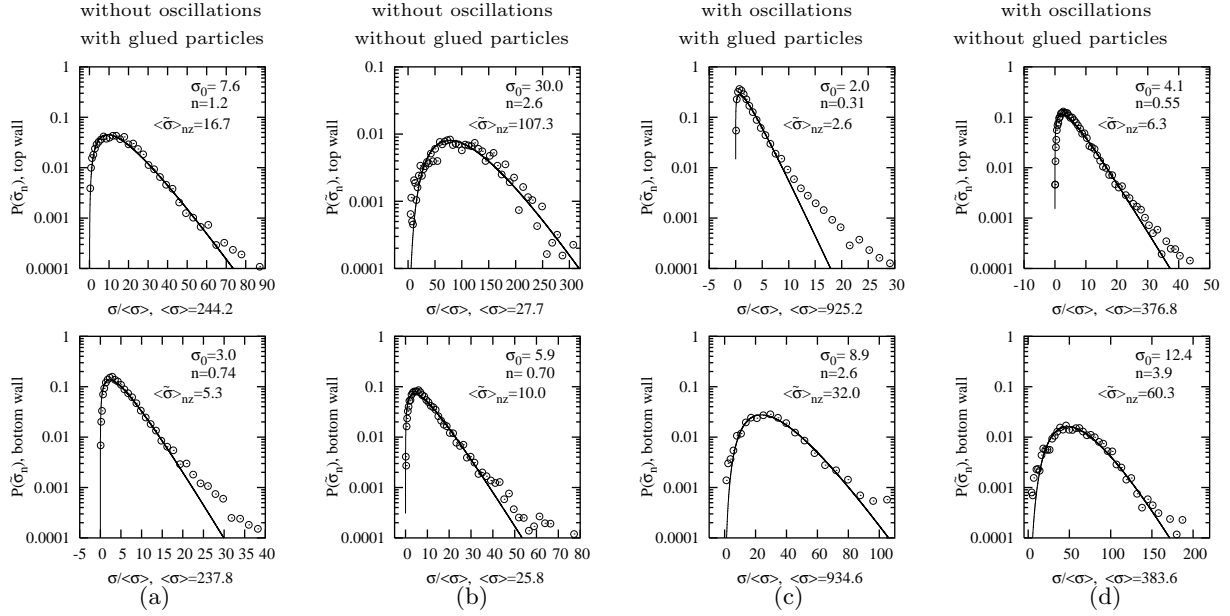
FIG. 14: Log plot of PDF for normal non-zero stresses on the top wall (top panel) and on the bottom wall (bottom panel) in typical configuration with four boundary conditions: (a) and (b) without oscillating bottom wall, (c) and (d) with oscillating bottom wall, (a) and (c) with glued particles, (b) and (d) without glued particles. Average normal stress per area $\langle\sigma\rangle$ is in units of $\rho_s\langle d\rangle^2/sec^2$. Solid lines: the best fits of the function (12), with the values of the fitting parameter n and corresponding σ_0 and $\langle\sigma\rangle_{nz}$ shown on each plot.

this regime, the width is determined by averaging effects and correlations, as we discuss later. On the other hand, in the case *zero stresses are present*, we have a significant dependence of the width of a distribution on the average non-zero stress $\langle\tilde{\sigma}\rangle_{nz}$. In a limiting case $\langle\tilde{\sigma}\rangle_{nz} \gg 1$, appropriate to most systems shown in Fig. 14, equation (19) reads:

$$\text{width} = \sqrt{\left(\frac{1}{1+n}+1\right)\langle\tilde{\sigma}\rangle_{nz}-1} \propto \sqrt{\langle\tilde{\sigma}\rangle_{nz}} \quad (20)$$

where we have used the fact that for $\langle\tilde{\sigma}\rangle_{nz} \gg 1$ sensors do not register more then one particle at a time and for single particle contacts $n = $ constant, as explained in next Section. Equation (20) is consistent with visual estimate of the widths of the distributions in Fig. 14: The larger $\langle\tilde{\sigma}\rangle_{nz}$ (shown in the right top area on each plot), the wider is the distribution. Next we show that $\langle\tilde{\sigma}\rangle_{nz}$ in turn depends on the collision rate, area of the sensors and averaging time.

Let $N_t = n_s n_T$ be the total number of stress measurements, obtained from all n_s sensors during n_T time-intervals. Out of N_t stresses, $N_{nz} \leq N_t$ are non-zero. The non-zero average stress depends on the size of sensor A_s and averaging time Δt,

$$\langle\tilde{\sigma}\rangle_{nz} = \frac{\langle\sigma\rangle_{nz}}{\langle\sigma\rangle} = \frac{N_t}{N_{nz}} = \frac{1}{w\,A_s\,\Delta t} \quad (21)$$

where w is the frequency of non-zero stress events per unit area. In the case of low collision rate with the sensors, when no more then one particle strikes A_s during

Δt, w has a meaning of particle-wall collision rate per unit area.

Relations (20) and (21) allow us to explain the distributions in Fig. 14. The sensor areas and averaging times are fixed so it is the rate of non-zero events w which determines the average and width of a distribution. To the first approximation $w \propto$ the volume fraction close to the respective boundary. From Fig. 4 (top panel), in the systems without oscillations the volume fraction is smaller at the top wall compared to the bottom wall. Therefore, the distributions are wider at the top compared to the bottom. In the systems with oscillations the volume fraction is smaller at the bottom wall compared to the top wall, therefore, the distributions are wider at the bottom.

2. Averaging effects

In this section we study one of the factors that can affect the parameter n, *i.e.* the number of contacts, N, between the particles and a sensor during the averaging time Δt.

Let us define the parameter n_0 that is characteristic for the distribution of stresses due to single particle contacts:

$$P_N(\tilde{\sigma}) = c\tilde{\sigma}^{n_0}e^{-\tilde{\sigma}/\sigma_0}; \qquad N = 1 \quad (22)$$

If more then one particle collide with the sensor of area A_s during time Δt ($N > 1$), then the stress distribution is different due to *averaging effects*. For instance, when two particles strike the same sensor during Δt, $N = 2$,

the probability of registering total stress F depends on the probability of one of them contributing the stress $\sigma \leq F$ and another one the stress $F - \sigma$. Assuming both considered particles have independent distributions (22), the distribution of their collective stress F is $P_2(F) = \int_0^F P(\sigma)P(F-\sigma)d\sigma$. Using (22) and the integral identity

$$\int_0^F \sigma^r (F-\sigma)^q d\sigma = F^{(r+q+1)}\,\Gamma(r+1)\Gamma(q+1)/\Gamma(r+q+2) \tag{23}$$

valid for any positive real numbers r and q, and in particular for $r = q = n_0$, we arrive at the following distribution for the stresses generated by double strikes:

$$P_2(\tilde{F}) = c_2 \tilde{F}^{(2n_0+1)} e^{-\tilde{F}/\sigma_0}; \ \tilde{F} = F/\langle\sigma\rangle \tag{24}$$

where c_2 is a normalization coefficient. Applying the same argument to the case when N particles strike the sensor during Δt we obtain the following distribution of stresses:

$$P_N(\tilde{\sigma}) = c\tilde{\sigma}^{(N(n_0+1)-1)} e^{-\tilde{\sigma}/\sigma_0} \tag{25}$$

The above calculation sets the relation between the parameter n and the number N as $n = N(n_0 + 1) - 1$, see (12). Therefore, under the assumption that particles are not correlated we obtain that the distributions of stresses generated by multiples collisions are characterized by higher power n. We will see below that this assumption is justified for the results shown in Fig. 14.

This conclusion may be used to explain the increased values of n observed in the distribution of stresses on the bottom wall in the systems shown in Fig. 14(c) and Fig. 14(d). In these systems the bottom wall is vibrated and most of the stress data are collected during the phase when the bottom is rising up. This phase is definitely characterized by increased compaction of particles close to the sensors and an increased number N.

However, an increase of N cannot be responsible for the large n's observed on the top wall in the system shown in Fig. 14(b), and, to lesser extend, Fig. 14(a). In particular regarding Fig. 14(b), we expect that the source of large n lies in the separately verified result that the typical normal components of the velocities of the particles colliding with the top wall is large, leading to different stress distribution. We note, however, that the values of n given in Fig. 14(a-b) are not as accurate as the rest of n's shown in Fig. 14 due to small volume fraction there (see Fig. 4(a-b)). Therefore, the number of collisions is small – e.g., we count approximately 500 collisions during the whole time span of the simulations presented in Fig. 14(b).

The results of Fig. 14 allow us to estimate the parameter n_0 defined earlier in this Section as the value of n corresponding to the distribution of stresses registered by the sensors with $N = 1$. Because $n_0 \leq n$ (see (25)), the smallest found n provides an upper bound on n_0. The lowest values of n are found in the distributions shown in Fig. 14: (a) bottom, (b) bottom, (c) top and (d) top. For these cases $n < 1$, therefore $n_0 < 1$. This result is very different from $n_0 = 2$ in the q-model: this should be no surprise because q-model assumes high volume fraction and static configuration.

3. Correlations

The dependence of the normal stress distributions on the number of contacts per sensor can be described by (25) only when the particles participating in contact with a sensor are not correlated. However, there are certain regimes and conditions of granular flow when this assumption may not be correct. For example, Miller, O'Hern and Behringer[26] studied the response of the force distribution to the number N, controlled in their case by the size of particles, and found that in dense granular flow the distribution widths were approximately independent of N. This independence was attributed to the presence of correlations due to presence of force chains.

In what follows we present the systematic study of the effect of sensor size (and, hence, the number N) on the bottom wall stress distributions for our typical configuration without oscillations and with glued particles, Fig. 4(a). This study will allow us to confirm the validity of our predictions (19) and (25) in a more quantitative way and to check for possible correlations.

In order to explore large range of sensor sizes, here we use *sector-shaped* sensors, obtained by dividing the bottom wall area by a number of radial lines drawn from the center of the cell toward outside boundary, see Fig. 13(b). Each sensor has the same radial dimension equal to the distance between the inner and outer cylinder, and the same angular dimension, set to the values $2\pi/m$, $m \in [2, 252]$. Therefore, the area of sector-shaped sensors varies between 1.0 and 125.6 (in units of $\langle d \rangle^2$), with the largest sensor being half of the bottom wall. For selected values of sensor areas we have confirmed that the results do not depend on the sensor shape. We note that all the results presented so far were obtained using small sensors of the area $1.19\,\langle d \rangle^2$.

Figure 15(a) shows the results for width of distribution (15) as a function of A_s for fixed values of δt in the range between $T_w/100 = 0.0002\,sec$ and $20\,T_w = 0.5463$. This range includes our typical value $\Delta t = T_w/10 = 0.0027$ (open triangles) used to obtain the distributions in Fig 14. To help interpretation of the results, we plot in Fig. 15(b) the value of $\langle\tilde{\sigma}\rangle_{nz}$, in Fig. 15(c) the average number of contacts per sensor, and in Fig. 15(d) the widths of distributions versus the product of the averaging time and the sensor area.

This figure shows that if zero stresses are present, i.e. $\langle\tilde{\sigma}\rangle_{nz} > 1$, the widths scale with the sensor area as $A_s^{-0.5}$, which is the scaling predicted by (20). This result applies to all sensor sizes when $\Delta t = 0.0002\,sec$, to the sensors of $A_s < 20$ when $\Delta t = 0.0027\,sec$, and to the sensors of $A_s < 2$ when $\Delta t = 0.0273\,sec$, see Fig. 15(b).

When zero stresses are not present ($\langle\tilde{\sigma}\rangle_{nz} = 1$) the
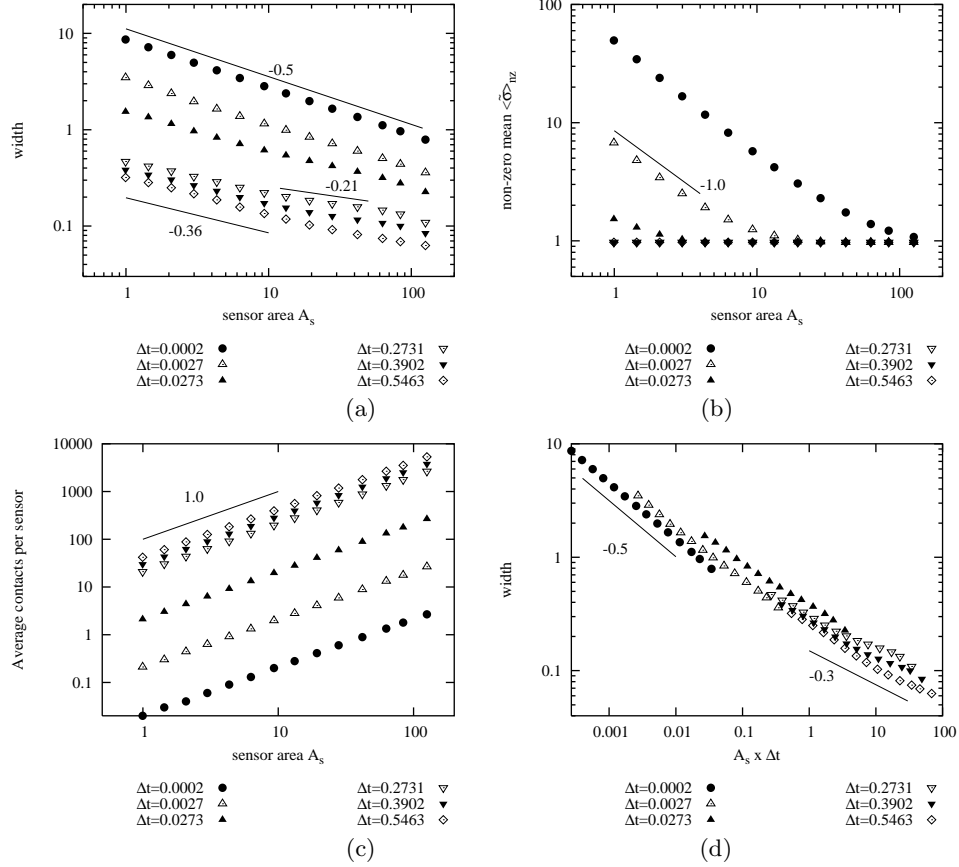
FIG. 15: (a) The widths of force distributions as defined by (15) versus the sensor area A_s (in units of $\langle d \rangle^2$) for six values of Δt (shown below the plot). (b) Average non-zero stress $\langle \tilde{\sigma} \rangle_{nz}$ as a function of A_s for the same six averaging times (for $\Delta t \geq 0.2731$ $\langle \tilde{\sigma} \rangle_{nz} = 1$). (d) Average number of contacts per sensor as a function of A_s. (c) Collapse of the width data against the product $\Delta t A_s$. The solid lines have specified slopes.

width (19) reduces to:

$$\text{width} = \sqrt{\sigma_0} = (N(n_0 + 1))^{-0.5} \qquad (26)$$

Here $N \propto A_s$ is a number of contacts per sensor from (25) and absence of correlations is assumed. This relation (26) is consistent with the $A_s^{-0.5}$ in Fig. 15(a) in the case $\Delta t = 0.0027\,sec$ and $A_s > 20$. However, when $\Delta t \geq 0.0273$ (for these large Δt's, the zero stresses are absent for almost all considered sensors, see Fig. 15(b)) the widths decrease with an increase of A_s at a slower rate then predicted by (26). We observe the slowest decrease, approximately $A_s^{-0.21}$, for the sensor sizes $10 < A_s < 100$, and for the averaging times of $0.2731\,sec$.

We expect that the origin of this slower decrease of the widths is the presence of correlations between the particles striking the same sensor (which may include self-correlation, i.e., the same particle colliding with a same sensor on multiple occasions during a given Δt). For example, the distribution of stresses due to N completely correlated particles acting on each sensor would have $n = n_0$, leading to the widths independent of A_s. Therefore, the stronger are the correlations between particles, the lower is the exponent in the width versus A_s

function. In Fig. 15(a) we can see that stronger correlation effects (*i.e.* slower decrease of the widths with an increase of A_s) occur for longer Δt and larger A_s. This is even more evident when the width is plotted against the product Δt times A_s, see Fig. 15(d): the slope changes gradually from -0.5 for small $\Delta t\, A_s$ to about -0.3 for large $\Delta t\, A_s$. The collapse of almost all data points on approximately single curve in Fig. 15(d) indicates the fact that the same averaging or correlation effects result if either Δt or A_s is increased by the same factor. Possible exception to this rule are very long Δt's, which we discuss below.

We note that Miller, O'Hern and Behringer,[26] have found evidences of strong correlations when they estimated experimentally the *width* $\propto A_s^0$ for $\Delta t = 0.0005\,sec$ and $5 \leq A_s \leq 80$. However the overall volume fraction of their samples was considerably higher (because of the heavy top wall supported in gravitational field by the granular material), therefore the spatial correlations can be explained if one assumes the normal stress on the bottom wall is applied through the network of *force chains*.[36] The results presented here are obtained for smaller volume fraction and in the absence of gravity.

However, in our case we expect that spatial correlations may arise from statistical fluctuations of the local volume fraction. These fluctuations lead to occasional formation of the denser structures of particles, stretched from the top to bottom wall: the presence of friction between the particles insures the lifetime of these formations is relatively long. As in the case of force chains, the dense structures carry more stress then the "free" particles in the "inter-structure" space, thus introducing spatial correlations. Unlike the force chains, the dense structures do not form dense force network and are not present always. They may form and disappear allowing for longer "structure-free" periods. This concept is consistent with the fact that our correlations are weak and the correlation regimes are detected only when Δt and A_s are large enough to include such a structure event. In addition the average number of contacts with sensors, see Fig. 15(c), is larger then 10 in the regimes where (26) fails. This fact suggest the possibility of *frequent returning contacts* of the same particle with a sensor, which in event-driven simulations is a signature of a particle pressed to the sensor from above, as one would expect for a particle that is member of a dense structure. The existence of similar structures (named as "transient force chains") was also suggested in Ref. 30.

We note that the dependence of the width on A_s becomes stronger again in the case of very long Δt's, see the results for $\Delta t = 0.5463$ in Fig. 15(a). Simple estimate shows that this change in trend occurs when Δt is so long that a typical particle, moving with a typical velocity, travels across a sensor in the time that is shorter than Δt, therefore decreasing this self-correlating effect. We currently investigate the scenarios proposed here in more detail and plan to present the results elsewhere.

B. Tangential stress distributions

Tangential (shear) stress is defined by (9). Figure 16 shows the tangential stress distributions (filled triangles) scaled by mean tangential stress, $\tilde{\sigma} = \sigma_t/\langle\sigma_t\rangle$ for the same boundary conditions as discussed in Fig. 14. For the convenience of comparison, the normal stress distributions from Fig. 14 are also shown (open circles).

The average tangential stress, shown in the horizontal label on each plot, is positive on the top wall and negative on the bottom. This reflects the fact that the top wall is mostly accelerating the particles while the bottom wall is slowing them down. The absolute value of the average tangential stress $\langle\sigma_t\rangle$ tells us the magnitude of torque and power needed to keep the top wall rotating and the bottom wall stationary. It is considerably larger for the systems with glued particles compared to the ones without glued particles, since the glued particles enhance momentum exchange between the wall and the free particles. We also note that $|\langle\sigma_t\rangle|$ is larger on the top wall then on the bottom by a factor of 3 for the systems without oscillations, and by a factor of 5

for the systems with oscillations. This factor is larger in the latter system since oscillations increase the vertical velocity fluctuations and the dissipation of the momentum on the sidewalls is increased. Since the momentum conservation requires that the momentum applied to the system through the top wall be equal to the momentum dissipated on both sidewalls and on the bottom wall, less momentum is left for the bottom wall in the systems with oscillations.

Similarly to the normal stresses, we observe the exponential tails for $\tilde{\sigma} > \tilde{\sigma}_0$ where $\tilde{\sigma}_0$ is the location of the peak of a distribution. For most considered cases, these tails have the same slope and location as the tails of the normal stresses. This suggests strong correlation between the normal and tangential stresses. However, for $\tilde{\sigma} < \tilde{\sigma}_0$ the distribution of tangential stresses differs qualitatively from the distribution of normal stresses. The PDF's of tangential stresses decrease to zero in an exponential manner, allowing for stresses in the direction opposite $\langle\sigma_t\rangle$. However, in most cases this different behavior has only weak influence on the width of the distributions.

An exception is the case of oscillating bottom wall (Fig. 16(c) and (d) bottom panel) where the tangential distributions are noticeably wider then the normal stress distribution. This can be explained by noticing that when bottom is moving up, the particles next to the bottom wall are constrained by increased volume fraction to move predominantly in the horizontal directions, therefore increasing fluctuations of tangential stresses.

To better understand the relation between the normal and tangential stresses we study in more details the time series of these stresses. Figure 17, top two panels, shows the values of $\sigma_n/\langle\sigma_n\rangle$ and $\sigma_t/\langle\sigma_t\rangle$ as a function of time registered by a single sensor on the bottom wall for the four boundary conditions as in Fig. 16. Simple visual inspection of Fig. 17, top two panels, shows that the normal and tangential stresses are correlated. This observation is confirmed by comparing the normal stress autocorrelation function with the appropriate cross-correlation function, as we discuss next.

Consider the time signals $\tilde{\sigma}_n(t)$ and $\tilde{\sigma}_t(t)$ shown in Fig. 17, first and second panels. If these signals are correlated then we can write

$$\tilde{\sigma}_t(t) = K\,\tilde{\sigma}_n(t) + R(t), \tag{27}$$

where $R(t)$ is a noise term such that $\langle R \rangle = 0$ and $K = \langle\tilde{\sigma}_t\rangle/\langle\tilde{\sigma}_n\rangle = 1$. Then the cross-correlation function defined as $\langle\tilde{\sigma}_n(t_0)\tilde{\sigma}_t(t_0 + t)\rangle$ must be equal to the autocorrelation function defined as $\langle\tilde{\sigma}_n(t_0)\tilde{\sigma}_n(t_0+t)\rangle$. In the definition of these time correlation functions, averaging is performed over all initial times t_0. To reduce noise we also average the results of all sensors.

Figure 17, third panel, shows that to within small error $\langle\tilde{\sigma}_n\tilde{\sigma}_t\rangle = \langle\tilde{\sigma}_n\tilde{\sigma}_n\rangle$, therefore, confirming the relation (27) with $\langle R \rangle = 0$. This figure also shows that the correlation functions decay very fast within an interval shorter than averaging time. For longer times, the correlation
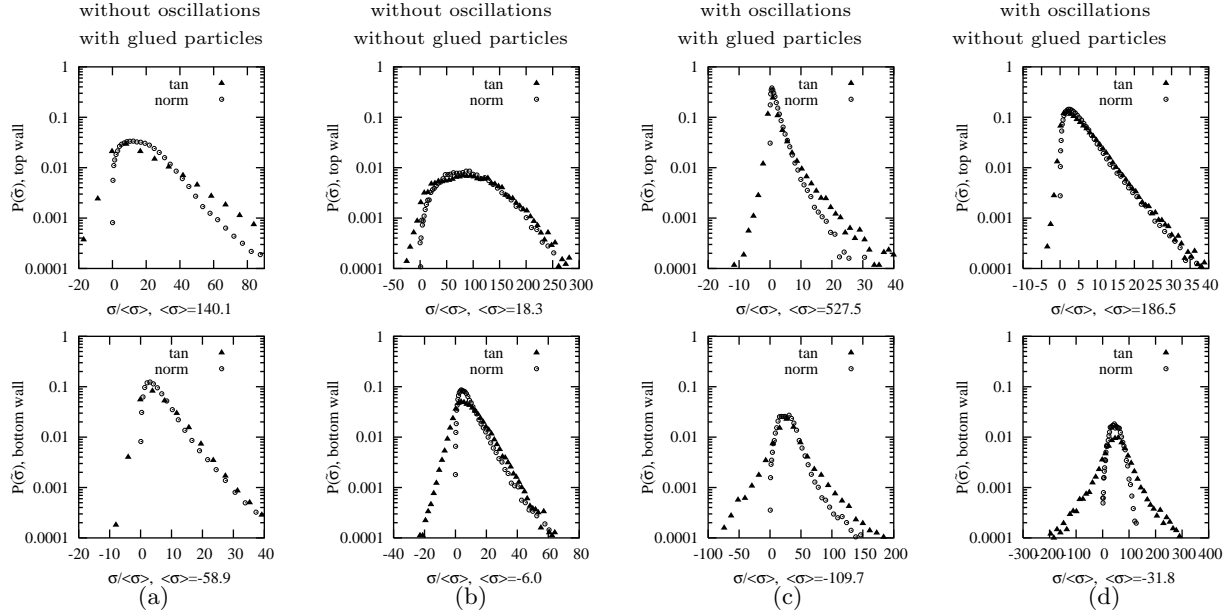
FIG. 16: Log plot of PDF for tangential non-zero stresses (filled triangles) on the top wall (top panel) and on the bottom wall (bottom panel) in the typical configuration with four boundary conditions: (a) and (b) without oscillating bottom wall, (c) and (d) with oscillating bottom wall, (a) and (c) with glued particles, (b) and (d) without glued particles. Average tangential stress per area $\langle \sigma \rangle = \langle \sigma_t \rangle$ is in units of $\rho_s \langle d \rangle^2 / sec^2$. For comparison, normal stress distributions from Fig. 14 are replotted here (open circles).

function decreases until it reaches its uncorrelated value equal to unity in the systems without oscillations, (a) and (b), and it oscillates around this uncorrelated value with the frequency of driving oscillations for (c) and (d). We note that larger particle velocities lead to faster decay of correlation functions in Fig. 17(a) compared to 17(b) (see also Fig. 4(a-b), top panel). The uncorrelated value for both correlation functions is equal to unity because an average of product of two uncorrelated stresses is equal to the product of average stresses.

The results of this section confirm strong correlation between the normal and tangential stresses. This correlation renders that many conclusions obtained for normal stresses also apply to the tangential stresses.

V. CONSTANT VOLUME VERSUS CONSTANT PRESSURE SIMULATIONS

All the results we have discussed so far are obtained for the systems characterized either by fixed constant volume, as in the simulations without oscillations, or by prescribed volume dependence on time, as in the simulations with oscillating bottom wall. We refer to these cases as *controlled volume simulations*. A special case of controlled volume simulations are the *constant volume (CV) simulations* where the volume of the system is kept strictly constant (no oscillations).

It is, however, well known, that the volume constraint can significantly affect the granular flow at high volume fractions. The system can be easily locked in a jammed state. That is why dense sheared granular flow experiments are commonly carried out using adjustable volume, but controlled pressure. Miller, O'Hern and Behringer,[26] for example, report the results for the sheared granular flow in a Couette cell, where the weight of the top wall provides constant pressure. Also, all free surface granular flows in gravitational field, for example, the flow of the granular matter down an inclined plane,[5,37] are the examples of controlled pressure scenarios. In these cases the weight of the granular matter itself controls the pressure both inside the system and on the boundaries. Recently, new studies emerged that indicated the importance of the difference between controlled volume and controlled stress boundary conditions. For example, Aharonov and Sparks[2,38] use the 2D numerical simulations to study the response of the dense sheared granular system to the applied boundary pressure. They find different shearing modes determined by pressure; These modes can have very similar volume fractions, but different microstructural organization.

In this section we describe the simulations of sheared granular flow in a system where the pressure on one of the walls is controlled at all times. We refer to these boundary conditions as *controlled pressure simulations*. When pressure is kept constant we have the case of *constant pressure (CP) simulations*. In laboratory experiments the CP condition can be realized not only by setting the constant weight load on a movable top wall of a Couette cell[26], but also by setting the movable wall, for example, a bottom wall, on a compressed spring, see Fig. 18 and Ref. 22. Any increase of the pressure inside the cell
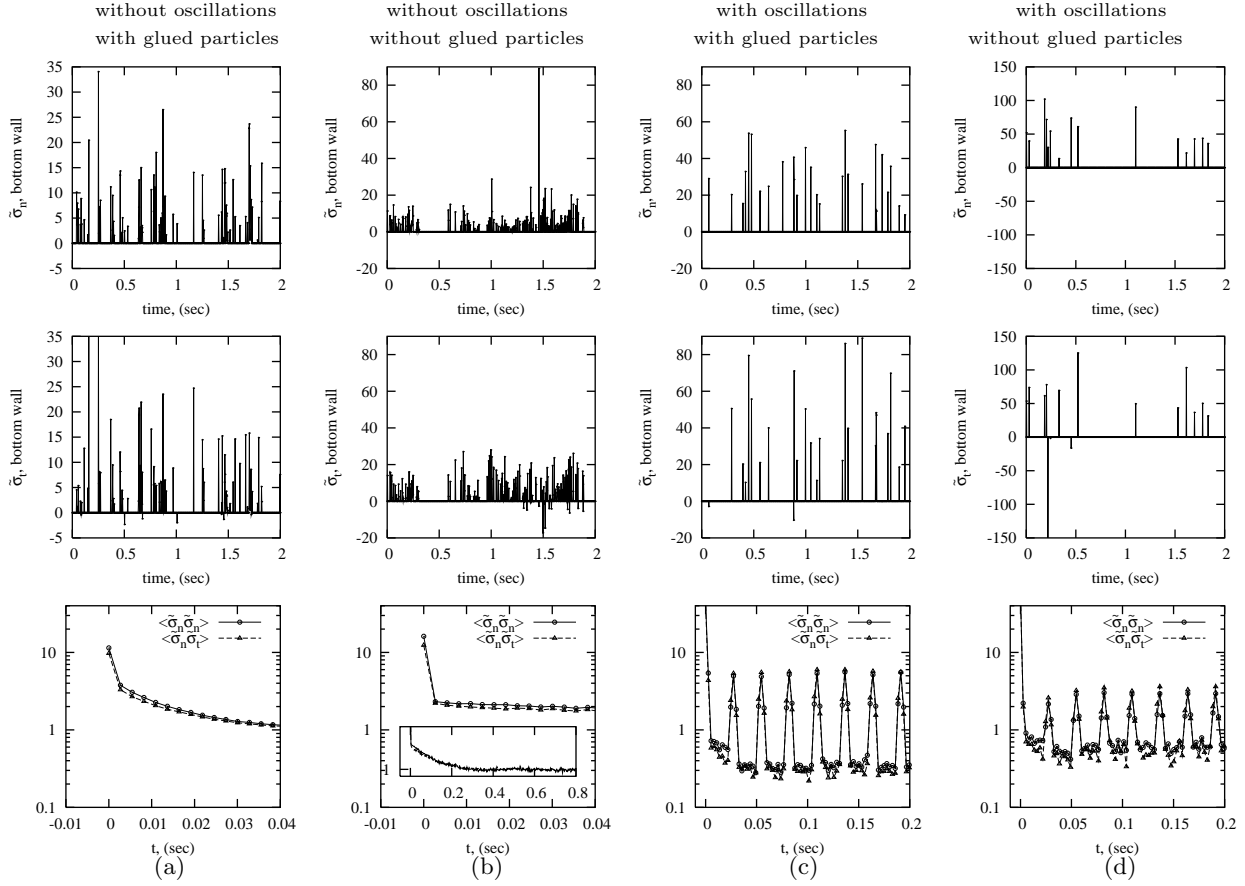
FIG. 17: First panel: normal stress signal on the bottom wall during randomly chosen interval of 2 seconds. Second panel: tangential stress signal on the bottom wall for the same 2 seconds interval. Third panel: stress auto- and cross-correlation functions. The inset in (b) shows the correlation functions on the longer time scale. (a) and (b) - without oscillating bottom wall, (c) and (d) - with oscillating bottom wall, (a) and (c) - with glued particles, (b) and (d) - without glued particles.
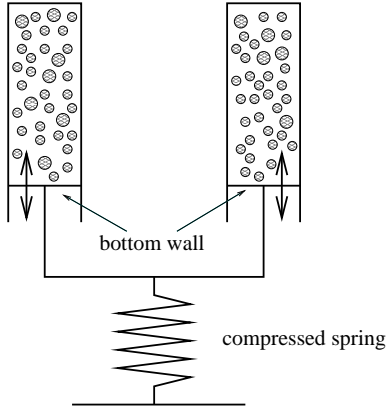

FIG. 18: Schematic representation of Couette cell in vertical cross-section with movable bottom wall: possible realization of constant pressure experiment.

results in an increase of the volume of the cell and vice versa. The compressed spring realization is especially relevant if the experiment is conducted in zero gravity.

In numerical simulations we adopt the following algo-

rithm (which is an approximation of a compressed string) to control the pressure. The whole timespan of simulation is divided into small time intervals $\Delta\tau$. At the beginning of each time interval we calculate the total stress on the bottom wall, σ, using the impacts of the particles during the previous time interval. More precisely, we use Eq. (8) with $A_s = A_{base}$ and put $\Delta t = \Delta\tau$. We then compute the vertical velocity of the bottom wall, v_b, as follows:

$$v_b = \begin{cases} -\bar{v}_b, & \sigma > \bar{\sigma} + \delta\sigma/2 \\ 0, & \bar{\sigma} - \delta\sigma/2 < \sigma < \bar{\sigma} + \delta\sigma/2 \\ +\bar{v}_b, & \sigma < \bar{\sigma} - \delta\sigma/2 \end{cases} \qquad (28)$$

where $\bar{\sigma}$ and $\delta\sigma$ are the prescribed stress and stress tolerance, and $\bar{v}_b$ is a prescribed maximum instantaneous velocity of the bottom wall. Within each time interval $\Delta\tau$ we run the controlled volume simulations with constant velocity of the bottom wall given by Eq. (28). The resulting changes of the volume of the cell adjust the stress back to the prescribed value. This model leads to vibration of the bottom wall in steady state; similar vibrations are also observed in experiments.[39]

We consider the system without oscillations and with glued particles on the top wall, Fig. 4(a), as a basis for all our CP simulations. We set the constant stress on the bottom wall being equal to the average stress $\langle \sigma_n \rangle$ on this wall which we measured in CV simulations with $V = 10 \, rad/sec$. The choice of the parameters used in the model (28) is

$$\bar{\sigma} = 222 \, \rho_s \frac{\langle d \rangle^2}{sec^2} \qquad (29)$$

$$\delta\sigma = 20 \, \rho_s \frac{\langle d \rangle^2}{sec^2}$$

$$\Delta\tau = T_w/25$$

$$\bar{v}_b = \langle d \rangle / \Delta\tau / 1000 = 0.915 \langle d \rangle / sec \qquad (30)$$

Figure 19(a) shows the PDF for the stresses on the complete bottom wall in the case of CP simulations (circles) using parameters given by (29)-(30) and $\Delta t = \Delta\tau$. For comparison, the results of CV simulations for the same A_s and Δt are shown on the same plot (triangles). We see that the CP distribution is wider compared to CV case. To understand this difference it is useful to distinguish three sets of collected stress data, each set containing the data from one of three phases of the bottom wall motion: moving up, staying put, and moving down (this separation of the stresses is possible only because $\Delta t = \Delta\tau$, *i.e.* during the averaging time the bottom wall does not change its velocity). In each phase we have controlled volume evolution of the system with a different mean stress: highest in the phase of the bottom wall moving up and lowest in the phase of the bottom wall moving down. The resulting CP distribution must correspond to the superposition of the distributions from three phases. The degree of widening of the stress distribution can be estimated using the following argument.

If $\Delta v_y^{(CV)}$ is a change in the normal component of velocity of a particle interacting with a stationary sensor and $\Delta v_y^{(CP)}$ is a change in the normal component of the velocity of the same particle interacting with a sensor that has the velocity v_b, then $\Delta v_y^{(CP)} = \Delta v_y^{(CV)} + v_b$ (note that v_b can take three different values, see (28)). If we have N particles of average diameter $\langle d \rangle$ interacting with a sensor A_s during Δt then, using the definition (8),

$$\sigma_n^{(CP)} = \sigma_n^{(CV)} + K_1 \frac{N v_b}{A_s \Delta t} \qquad (31)$$

where $\sigma_n^{(CP)}$ is a stress on a moving sensor, $\sigma_n^{(CV)}$ is a stress on a stationary sensor, and $K_1 = \frac{1}{6} \pi \rho_s \langle d \rangle^3$. Therefore, one expect that the distribution of $\sigma_n^{(CP)}$ is approximately $2 K_1 \frac{N v_b}{A_s \Delta t}$ wider then the distribution of $\sigma_n^{(CV)}$. This argument predicts that $(width^{CP} - width^{CV})/width^{CV} \sim 0.1 - 0.2$, consistently with the results shown in Fig. 19(a) (in the estimate we use $N = 10$, based on the results shown in Fig. 15(c)). We note that the above argument applies only to the normal stresses, since this is the direction of v_b.

In principle, both normal and tangential stresses can also be affected by the changes in the volume fraction and in the velocity profiles due to the motion of the bottom wall. To estimate possible influence of this motion, we note that it is characterized by the approximate frequency of $1/(2\Delta\tau) = 457 \, Hz$ and the amplitude of $\bar{v}_b \Delta\tau/2 = 0.0005 \langle d \rangle$. Despite high frequencies, the vibrations of such a small amplitude are not expected to significantly modify stress distributions, as also illustrated also by the Fig. 20.

Figure 20 shows stress PDF's on typical size sensors using our typical averaging time $\Delta t = T_w/10$. Comparing to the stresses in CV simulations, Fig. 14(a) and Fig. 16(a), we do not see any significant differences. This is because $\Delta t > \Delta\tau$, therefore, during the averaging time the velocity of the bottom wall can change once or twice, resulting in "averaging out" the effect of the bottom wall motion. Therefore, we conclude that the model specified by (28-30) is effective in keeping constant stress, while not modifying significantly stress distributions on the time scales of interest.

A. Bagnold scaling

In this section we investigate the effect of the shearing velocity V on the stresses. The relation between average normal stress and V under certain conditions takes the form of *Bagnold scaling*[40], where stresses increase with the square of the shear rate. This effect has been studied in both CP and CV settings.[3,5,23,39,41] The quadratic dependence of the stress on the shearing rate is observed for the granular flows at high shearing rates or for lower volume fractions, *i.e.* in the systems where particles are not involved in multiple elastic deformations.[6]

Figure 21(a) shows log-log plot of the mean normal stresses on the bottom wall versus V at CV setting for the system shown in Fig. 4(a), *i.e.* with glued particles on the top wall and no oscillations. For configurations of $\nu = 40\%$ and $\nu = 50\%$ these results confirm Bagnold scaling for the range of V's between 1 rad/sec and 35 rad/sec. (Note that the $\nu = 50\%$ initial state was obtained from the typical configuration by adjusting the height of the cell according to (6)). The data are fitted by the power function $\langle \sigma \rangle = a V^b$ with $a = 0.015$ and $b = 2.20 \pm 0.2$ for $\nu = 40\%$ and $a = 0.201$ and $b = 2.18 \pm 0.2$ for $\nu = 50\%$.

Figure 21(b) shows scaled velocity profiles for different V's in CV simulations. The profiles are higher for faster shearing. The origin of this dependence may be related to the effect of sidewalls on the sheared system. Indeed, when we shear the system with elastic and smooth sidewalls, Fig. 6, the profiles do not depend on V. Experimental studies[15] also confirm the independence of velocity profiles on V in the case boundary effects are significantly minimized. To explain these results we consider the dependence of restitution parameters on the particle's velocity in particle-sidewall interactions. The normal coefficient of restitution (4) depends on the normal
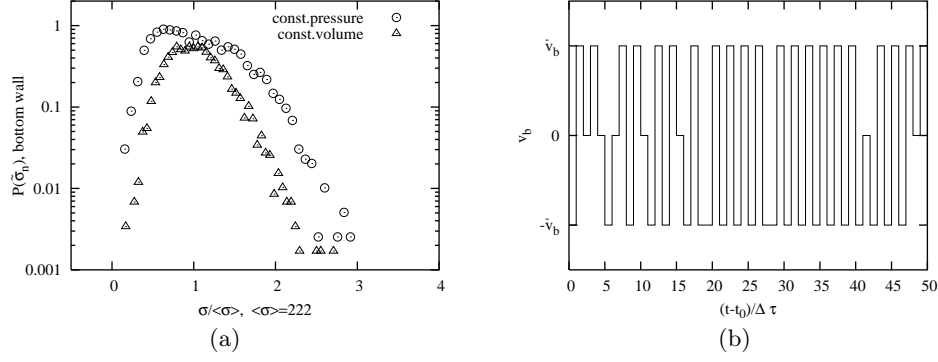
FIG. 19: (a) Stress on the base PDF for the case of CP simulations (circles), compared to CV results (triangles). Here $\Delta t = \Delta \tau = T_w/25$ and $A_s = A_{base}$ for both sets of results. (b) The velocity of the bottom wall in the CP simulations recorded after some late time t_0 in a steady state during 50 $\Delta \tau$ intervals.
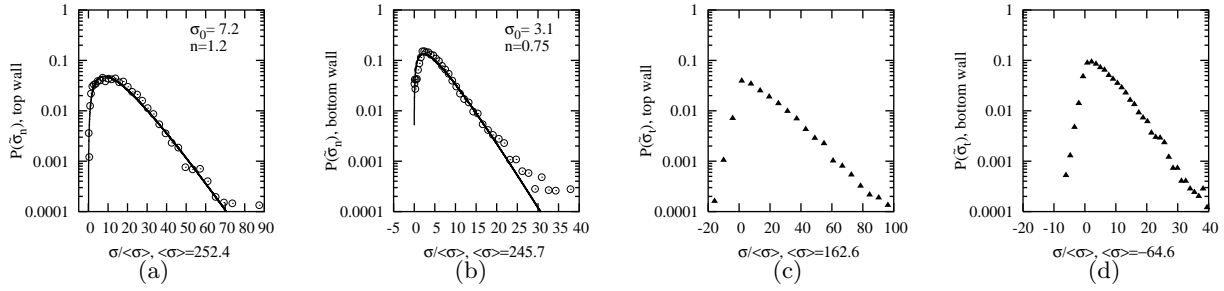

FIG. 20: Constant pressure simulations: Stresses for the case without oscillations and with glued particles on the top wall. Size of sensors $d_s = 1.09\langle d \rangle$. (a) (c) - sensors are on the top wall; (b) (d) - sensors are on the bottom wall; (a) (b) - normal stress PDF; (c) (d) - tangential stress PDF.
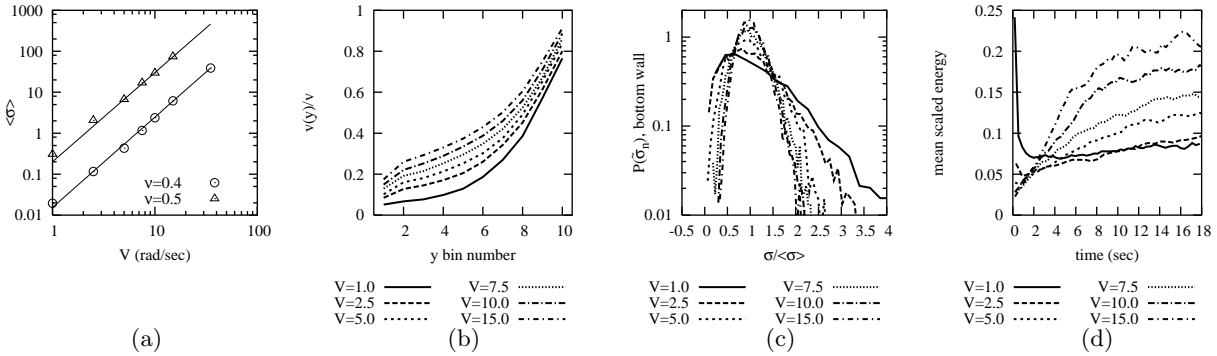

FIG. 21: CV simulations. (a) Stress as a function of V in log-log plot. Circles: $\nu = 40\%$. Triangles: $\nu = 50\%$. Solid lines are the best fits of power function as explained in the text. The rest of results shown is calculated using $\nu = 40\%$. (b) Velocity profiles; (c) Stress PDF, bottom wall, $\Delta t = T_w/25$. Measurements are taken over last $\Delta T = 5000\Delta t = 5.47 sec$ except for $V = 1 rad/sec$, where $\Delta T = 2sec$; (d) Scaled energy plots for different V's.

velocity of colliding particle; however this velocity is not influenced significantly by V. On the other hand, the coefficient of tangential restitution, β, in the case of sliding contacts (5) depends stronger on V since it involves the ratio of normal to tangential velocity, and the later scales with V. As it can be seen from (4), lower ratio has the same effect on dissipative mechanics as lower coefficient of friction, μ. Therefore, in the case of higher shear rates, the effect of sidewalls on the granular flow is

reduced, explaining the velocity profiles in Fig. 21(b).

The rest of the results shown in Fig. 21 includes stresses and mean scaled energies. We discuss them later in this Section in the context of comparative study of constant volume and constant pressure boundary conditions.

Next, we compare the effect of shearing velocity on the stresses for CV and CP configurations. In CP simulations we choose the fixed value of the stress on the
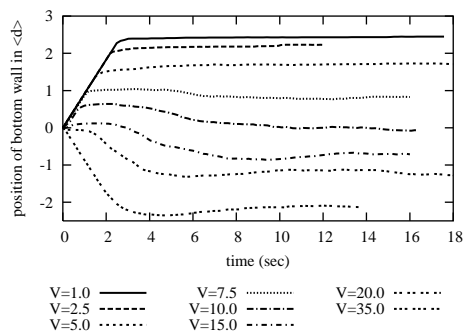
FIG. 22: Constant pressure simulations. Position of the bottom wall, h, (in units of $\langle d \rangle$) as a function of time for different shearing velocities.

bottom wall given by (29). Figure 22 shows the vertical position of the bottom wall h as a function of time for different V ($h = 0$ corresponds to the distance from the top wall equal to $10.54\langle d \rangle$). As expected, we see that slower/faster shearing leads to smaller/larger stress, and to an adjustment of the wall position occurring over some time interval (which is influenced by the "spring" parameters given by (29-30)). The stabilized (long time) wall positions are used to calculate ν for each V. Figure 23(a) shows resulting ν's. We notice significant change in ν as V is modified: ν at high shearing (35 rad/sec) is about 1.6 times smaller then ν at low shearing (1 rad/sec).

Figure 23(b) shows the effect of V on the velocity profiles. This result shows three types of different response to the increase of V in CP. For small V's, $V \leq 2.5\,rad/sec$, the shearing is stronger for larger V. For intermediate V's, $2.5\,rad/sec \leq V \leq 5\,rad/sec$ the velocity profiles are almost the same, and for $V \geq 5\,rad/sec$ the shearing decreases with an increase of V. These results can be understood in terms of the volume fraction, ν, as a determining factor. For the smallest V (solid line in Fig. 23(b)) ν is about 53%, therefore local jammed areas can be formed inside the sample reducing the overall mobility and shearing of the sample. These jammed areas can manifest themselves as "plateaus" in velocity profile. One such plateau can be seen in Fig. 23(b), solid line, between y numbers 4 and 5. As ν decreases with an increase of V, the sample gets more fluidized and the shearing improves. However, further increase of V and decrease of ν makes the system more "compressible": the dilation close to the top wall is stronger, reducing the momentum flux from the top wall to the bulk of the sample, resulting in weaker shearing. Therefore, the influence of V on a CP system is more complicated compared to a CV case, where velocity profiles are changing monotonously with V, see Fig. 21(b).

The distributions of the normal stress on the bottom wall are shown in Fig. 21(c) for the CV and in Fig. 23(c) for the CP. In both cases, CV and CP, the widths of distributions increase with a decrease of V. The distributions differ in the following: in CP case (Fig. 23(c)) the distribution shows a double peak at low shearing around

the prescribed value of the stress; This double peak is absent in CV case. This double peak occurs since at low V the volume fraction is high, up to 52%. Thus the collision rate between the particles and the moving bottom wall is higher and, hence, larger momentum is transfered to the granular system. If this momentum is large enough, we have the situation in which the "restoring force" of the bottom wall brings the system in just one interval $\Delta\tau$ from the overstressed state to under-stressed state or vice versa. Therefore, the velocity of wall, (28), in steady state alternates its value between positive and negative without taking zero value, resulting in two peaks in stress distribution: one for overstressed state and another one for under-stressed state.

Finally, Fig. 23(d) shows the time evolution of the mean scaled energy of the system. This figure shows that for large V's, the equilibrating time decreases with an increase of V, while for low shearing this trend is opposite. This effect is due to the fact that the equilibrating time depends on the collision rate, which in turn is the function of V and ν. At high shearing ν changes slowly with shearing, see Fig. 23(a), so mostly V determines the collision rate, leading to the observed decrease of the equilibrating time with faster shearing. On the other hand, at slow shearing, small changes in V cause large changes in ν. Here mostly ν determines the collision rate, leading to the observed increase of the equilibrating time with faster shearing.

VI. CONCLUSIONS

The presented studies concentrate on 3D event driven simulations in the Couette geometry with top rotating wall and with physical boundary conditions in zero gravity. The velocity and volume fraction distributions are strongly dependent on various boundary conditions, such as: top shearing wall properties, side wall properties, presence of oscillations of the bottom wall, or intensity of shearing. The overall volume fraction of studied granular system is 40 %, however, the shearing and vibrating walls impose the non-uniformity in volume fraction dis-
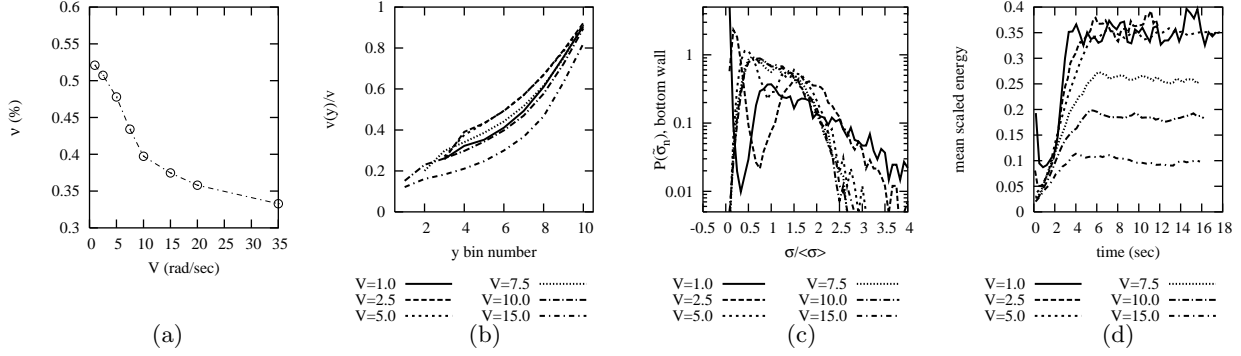
FIG. 23: CP simulations. (a) ν as a function of V; (b) velocity profiles; (c) Stress PDF, bottom wall. These distributions are obtained from the stress data taken every $\Delta t = \Delta\tau = T_w/25$ seconds over the last $\Delta T = 5000\Delta t$; (d) scaled energy plots.

tribution with the formation of high-dense band (cluster) where local volume fraction reaches up to 60%. The cluster can respond to shearing in different ways. For example, while very rough and inelastic top wall, but without glued particles, cannot induce any significant shearing when side-walls are dissipating, it imposes a shear and high tangential velocities of all particles in the case of smooth and elastic side-walls. Typically, inside the cluster the shear rate is very small. However, the presence of the glued particles on the top wall considerably increases shear rate inside this cluster.

The presence of oscillations of the bottom wall seems to have three effects: 1) the slippage velocity at the bottom increases. 2) the dense cluster is located further away from the bottom wall compared to the systems without oscillations. 3) equilibrating times to reach a steady state are shorter in the systems with oscillations due to the increased collision rate.

The equilibrating dynamics involves attaining the steady state values of volume fractions and velocities. The time scales of these two equilibrating processes are different: in most cases, steady state profile in volume fraction is attained very fast, while velocity profiles reach their final shape much later. However, the volume fraction distribution takes longer to reach a steady state when the rate of energy input due to shearing is low. This occurs in the systems without glued particles and without oscillations. For example, in so called "delayed dynamics" regime, described in Sec. III C, the time needed for the cluster to accumulate enough energy to dis-attach from the bottom wall can be very long. However, once this happens, the velocity profile changes drastically. More generally, these simulations show that the velocities and volume fractions strongly depend on boundary conditions: simulations using *e.g.* periodic boundary conditions may miss a number of interesting effects presented in this work.

We have also analyzed stress and stress fluctuations on the boundaries. We find that the distribution of normal stresses in a system of 40% volume fraction and rapid granular flow can be described by the same functional form (12) as used for stress distribution in static dense system, *i.e.* with power-law increase for small stresses and exponential decrease for large ones. Considering this functional form as a useful guide, we predict the behavior of main characteristics of stress distributions as a function of sensor area and averaging time. These predictions describe well the width of distributions for small sensors and short Δt's. However, they fail for large sensors and long averaging times, suggesting the existence of additional correlations not accounted by our functional form. The correlations may be related to the existence of "denser structures" in the simulated systems.

We simulate "constant pressure" boundary condition and we discuss the differences between the results in constant volume and constant pressure settings. A key observation here is very different reaction to an increase of shearing velocity in the system with constant pressure boundary condition compared to the systems with constant volume boundary condition. In the first case the shearing velocities are increasing because of the velocity dependence of the coefficients of restitution while in the second case they are initially increasing and then decreasing because of the changes of volume fraction with imposed shear.

* oleh.baran@njit.edu; http://math.njit.edu/~oleh/

[1] Movies of the simulations can be found at

`http://math.njit.edu/~oleh/shear_shake/`.

[2] Einat Aharonov and David Sparks. Shear profiles and localization in simulations of granular materials. *Phys. Rev. E*, 65:051302, 2002.

[3] C. S. Campbell and C. E. Brennen. Computer simulation of granular shear flows. *J. Fluid Mech.*, 151:167, 1985.

[4] C. S. Campbell. The stress tensor for simple shear flows of a granular material. *J. Fluid Mech.*, 203:449–473, 1989.

[5] Leonardo E. Silbert, Deniz Ertas, Gary S. Grest, Thomas C. Halsey, Dov Levine, and Steven J. Plimpton. Granular flow down an inclined plane: Bagnold scaling and rheology. *Phys. Rev. E*, 64:050802, 2001.

[6] Charles S. Campbell. Granular shear flows at the elastic limit. *J. Fluid Mech.*, 465:261–291, 2002.

[7] Meheboob Alam and Stefan Luding. Rheology of bidisperse granular mixtures via event-driven simulations. *J. Fluid Mech.*, 476:69–103, February 2003.

[8] Meheboob Alam and Stefan Luding. First normal stress difference and crystallization in a dense sheared granular fluid. *Phys. Fluids*, 15:2298, 2003.

[9] Meheboob Alam, Jeffrey T. Willits, Birgir O. Arnarson, and Stefan Luding. Kinetic theory of a binary mixture of nearly elastic disks with size and mass disparity. *Phys. Fluids*, 14:4085, 2002.

[10] M. Alam and P. R. Nott. Stability of plane couette flow of a granular material. *J. Fluid Mech.*, 377:99–136, 1998.

[11] P. R. Nott, M. Alam, K. Agrawal, R. Jackson, and S. Sundaresan. The effect of boundaries on the plane couette flow of granular materials: a bifurcation analysis. *J. Fluid Mech.*, 397:203–229, 1999.

[12] J. T. Jenkins and M. W. Richman. Boundary conditions for plane flows of smooth, nearly elastic, circular disks. *J. Fluid Mech.*, 171:313–328, 1986.

[13] M. Y. Louge, J. T. Jenkins, and M. A. Hopkins. Computer simulations of rapid granular shear flows between parallel bumpy boundaries. *Phys. Fluids*, 2(6):1042–1044, 1990.

[14] M. Y. Louge. Computer simulations of rapid granular flows of spheres interacting with a flat, frictional boundary. *Phys. Fluids*, 6(7):2253–2269, 1994.

[15] W. Losert, L. Bocquet, T. C. Lubensky, and J. P. Gollub. Particle dynamics in sheared granular matter. *Phys. Rev. Lett.*, 85:1428, 2000.

[16] B. D. Lubachevsky. Simulating billiards: Serially and in parallel. *Int. J. Computer Simulation*, 2:373–411, 1992.

[17] S. F. Foerster, M. Y. Louge, H. Chang, and K. Allia. Measurements of the collision properties of small spheres. *Phys. Fluids*, 6(3):1108–1115, 1994.

[18] W. Goldsmith. *IMPACT, The theory and physical behavior of colliding solids*. Edward Arnold, London, 1964.

[19] Thomas Schwager and Thorsten Pöschel. Coefficient of normal restitution of viscous particles and cooling rate of granular gases. *Phys. Rev. E*, 57:650, 1998.

[20] C. Bizon, M. D. Shattuck, J. B. Swift, W. D. McCormick, and H. L. Swinney. Patterns in 3d vertically oscillated granular layers: Simulation and experiment. *Phys. Rev. Lett.*, 80(1):57–60, 1998.

[21] O. R. Walton. Numerical simulation of inelastic, frictional particle-particle interactions. In M. C. Roco, editor, *Particulate two-phase flow*, page 884, Boston, 1993. Butterworth-Heinemann.

[22] Karen E. Daniels and Robert P. Behringer. Shearing and order in vibrationally fluidized 3d granular media. Private communications, 2004.

[23] S. B. Savage and D. J. Jeffrey. The stress tensor in a granular flow at high shear rates. *J. Fluid Mech.*, 110:255, 1981.

[24] J. T. Jenkins and S. B. Savage. A theory for the rapid flow of identical, smooth, nearly elastic, spherical particles. *J. Fluid Mech.*, 130:187–202, 1983.

[25] S. B. Savage. Analyses of slow high-concentration flows of granular materials. *J. Fluid Mech.*, 377:1–26, 1998.

[26] B. Miller, C. O'Hern, and R. P. Behringer. Stress fluctuations for continously sheared granular materials. *Phys. Rev. Lett.*, 77:3110–3113, 1996.

[27] C. Thornton. Force transmission in granular media. *Kona Powder and Particle*, 15:81–90, 1997.

[28] F. Radjai, M. Jean, J. J. Moreau, and S. Roux. Force distribution in dense two-dimensional granular systems. *Phys. Rev. Lett.*, 77(2):274, 1996.

[29] S. N. Coppersmith, C.-h. Liu, S. Majumdar, O. Narayan, and T. A. Witten. Model for force fluctuations in bead packs. *Phys. Rev. E*, 53(5):4673–4685, 1996.

[30] Emily Longhi, Nalini Easwar, and Narayanan Menon. Large force fluctuations in a flowing granular medium. *Phys. Rev. Lett.*, 89:045501, 2002.

[31] D. M. Mueth, H. M. Jaeger, and S. R. Nagel. Force distribution in a granular medium. *Phys. Rev. E.*, 57(3):3164–3169, 1998.

[32] C.-h. Liu, S. R. Nagel, D. A. Schecter, S. N. Coppersmith, S. Majumdar, O. Narayan, and T. A. Witten. Force fluctuations in bead packs. *Science*, 269:513, 1995.

[33] M. L. Nguyen and S. N. Coppersmith. Properties of layer-by-layer vector stochastic models of force fluctuations in granular materials. *Phys. Rev. E*, 59:5870, 1999.

[34] J. E. S. Socolar. Average stresses and force fluctuations in non-cohesive granular materials. *Phys. Rev. E.*, 57(3):3204–3215, 1998.

[35] S. F. Edwards and D. V. Grinev. Statistical mechanics of granular materials: stress propagation and distribution of contact forces. *Granular Matter*, 4:147–153, 2003.

[36] D. Howell and R. P. Behringer. Fluctuations in a 2d granular Couette experiment: A critical transition. *Phys. Rev. Lett.*, 82:5241, 1999.

[37] Michel Y. Louge and Stephen C. Keast. On dense granular flows down flat frictional inclines. *Phys. Fluids*, 13:1213, 2001.

[38] Einat Aharonov and David Sparks. Rigidity phase transition in granular packings. *Phys. Rev. E*, 60:6890–6896, 1999.

[39] S. B. Savage and M. Sayed. Stresses developed by dry cohesionless granular materials sheared in an annular shear cell. *J. Fluid Mech.*, 142:391–430, 1984.

[40] R. A. Bagnold. Experiments on a gravity-free dispersion of large solid spheres in a newtonian fluid under shear. *Proc. Royal Soc. London*, 225:49–63, 1954.

[41] G. Bossis, Y. Grasselli, and O. Volkova. Granular rheology in zero gravity. cond-mat/0309146, 2004.

[42] The important assumptions of theoretical models of stress distributions are the maintained contact between particles that are closely packed. These assumptions are valid in both completely static case and in the case of slow shearing at high density.